Electron and Exciton Dynamics at ZnO surfaces

AG Stähler
Department of Physical Chemistry
Fritz-Haber-Institute der Max-Planck-Gesellschaft

Clemens Richter

11 June - 11 December 2014

Contents

List of Figures

1 Introduction

The most common commercial optoelectronic devices such as light-emitting diodes (LEDs) or light-harvesting solar cells rely on inorganic semiconductors. The processing of semiconductors is often associated with high energy demand and costs and environmentally harmful byproducts. In order to diminish these unwanted side effects many efforts are taken in the development of devices based on organic semiconducting molecules/polymers, as they offer benefits like lower costs, lightweight, mechanical flexibility and wide chemical tunability. However, organic optoelectronic devices often suffer from lower performances and durability compared to their inorganic counterparts, which can be traced back to lower charge carrier mobilities in organic semiconductors and sensitivity toward water and oxygen. With the prospective to overcome these limitations, the combination of organic and inorganic semiconductors into hybrid structures not only promises the combination of the high carrier mobilities of inorganic semiconductors and the strong light-matter coupling of organic molecules, but also the emergence of novel physical properties. Since, this approach is based on the formation of an interface, the resulting device performance is strongly determined by the electronic coupling of both materials with respect to interfacial energy and/or charge transfer. These processes occur on ultrafast timescales. To investigate, understand and modify them, ultrafast time-resolution and surface sensitivity as well as model systems of controllable complexity and quality are desirable.

In this work, the polar, oxygen-terminated ZnO$(000\bar{1})$ surface and the spirobifluorene derivative SP6 were investigated under controlled ultra-high vacuum conditions with femtosecond time-resolved two-photon photoelectron (2PPE) spectroscopy.
The investigation started with the characterization of the electronic structure of the pristine ZnO$(000\bar{1})$ surface, followed by the study of the behavior upon hydrogen adsorption on the surface. Since hydrogen is an ubiquitious contaminant under experimental as well as industrial conditions, its influence on the ZnO$(000\bar{1})$ surface is crucial. As shown in Section 4.1 hydrogen leads to the modification of the surface electronic structure. Adsorption leads to the formation of a metallic surface state, the so called charge accumulation layer (CAL), by formation of highly polar, electron donating hydroxyl (OH) bonds at the surface. The buildup of the CAL was followed as a function of the hydrogen dosage and compared with results of a previous investigation of the nonpolar ZnO$(10\bar{1}0)$ surface. The

formation of the OH bonds at the surface enforces a downward bending of the conduction band minimum, which is initially bent upward, at the ZnO($000\bar{1}$) surface. Furthermore, time-resolved 2PPE experiments were performed to investigate the non-equilibrium dynamics induced by above band gap excitation. This technique enabled the observation of ultrafast electron relaxation in the conduction band and the formation of a long-living state which can be attributed to the formation of the surface exciton (SX). Comparison with the mixed-terminated ZnO($10\bar{1}0$) surface shows that modification of the CAL as a function of the H dosage, likewise renders the modification of the electron relaxation on both ZnO surfaces, suggesting that the observed dynamics might be determined by electronic effects rather than by structure.

In addition, the photoinduced dynamics of bulk-like films of SP6 on ZnO($10\bar{1}0$) were investigated with time-resolved photoemission. The PE signal obtained from these films, shows an unusual independence of the applied photon energies, which could be traced back to an emission by an intermolecular energy transfer between excited molecules. The origin of this signal could be ascribed to emission from a dark state (DS), which exceeds lifetimes of 25 µs and electrons from this state are emitted via strong coupling to the population of the first excited state S_1.

For further insight into the dynamics in SP6, test experiments to determine the mechanism of this intermolecular energy transfer and the strength of the coupling need to be performed. Moreover, with respect to hybrid systems, a detailed study of the electron dynamics at the SP6/ZnO($000\bar{1}$) as well as the SP6/ZnO($10\bar{1}0$) interface is necessary.

The presented investigation of the surface electronic structure and dynamics on the pristine and hydrogen-covered ZnO($000\bar{1}$) surface are crucial for the understanding of energy level alignment and electronic coupling of inorganic/organic interfaces. The appearance of a conducting charge accumulation layer, whose formation is most probable on the hydrocarbon-covered ZnO surface, is highly relevant for application of ZnO a transparent conduction electrode material. Further, the observed surface exciton might be used for highly distance-dependent interfacial energy transfer processes. The preliminary results on the photoinduced dynamics in SP6 provide information on the absolute energy levels of the bulk material, which is essential for interface energy level alignment. Moreover, the strong coupling of the excited states S_1 and DS, leading to a charge separation, possibly renders chances for light harvesting applications.

2 Theoretical background

2.1 Electron energetics at surface: workfunction, surface potential

When considering the electronic structure and dynamics at inorganic/organic interfaces, it is essential to understand the concepts of electron energetics at solid state surfaces. Here the workfunction is of high relevance in the scope of energy level alignment and ultrafast dynamics.

The workfunction Φ is a surface-specific property of every solid state material. Expressed in energetic terms, it is the energy difference between the Fermi level E_F, the electrochemical potential of electrons at finite temperatures, and the vacuum level E_vac, the potential of a free electron in the vacuum:

$$\Phi = E_\mathrm{vac} - E_\mathrm{F}. \tag{2.1.1}$$

Or in other words, Φ is the minimum amount of energy to overcome the potential barrier at the surface to remove an electron from the solid into the vacuum just outside the solid. This potential barrier of the solid/vacuum interface is schematically depicted in Figure 2.1.1(a). It is strongly influence by the non-zero dipole moment at the surface, which arises from the "spill-out effect", the non-zero electron density $\rho(z)$ directly outside of the surface. This is the consequence of introducing a surface to an infinite, periodic solid in three dimension. This situation is shown in Figure 2.1.1(b).

The upper part (a) in Figure 2.1.1 shows the potential distribution $\varphi(z)$ at the vacuum interface and the lower part (b) depicts the charge density distribution $\rho(z)$ at the surface. Due to the spatial extend of the electronic wave function the electron's probability density is non-zero in the vacuum where the positive ion cores are missing. Thus electron density can "spill out" of the surface and create a negative charge at the surface. In this case charge neutrality requires positive charge, which is realised by a rearrangement of electrons near the material's surface. While net charge neutrality is maintained, the surface possesses a finite dipole moment. Excited electrons face this dipole barrier on their way out into the vacuum. The strength of this dipole is characteristic for every surface and results in a varying workfunction for different surfaces of the same bulk material.

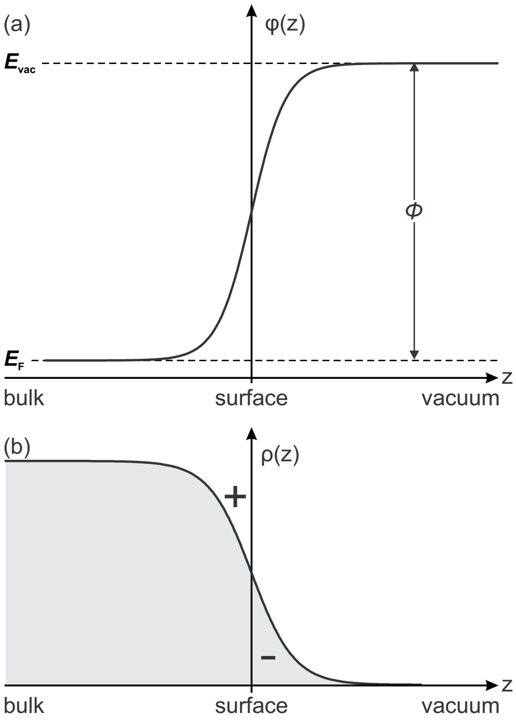

Figure 2.1.1: (a) Workfunction depicted as surface potential barrier (b) spill-out effect and resulting non-zero dipole moment at the surface.

An essential point in the investigation of surfaces, especially in the view of organic/inorganic hybrid systems, is the controlled modification of this surface dipole, respectively the workfunction, in the view of energy alignment. The adsorption of atoms or molecules on the surface directly affects the net surface dipole and either enhances or reduces it.

As an example, Figure 2.1.2 schematically depicts the influence of H adsorption. In Figure

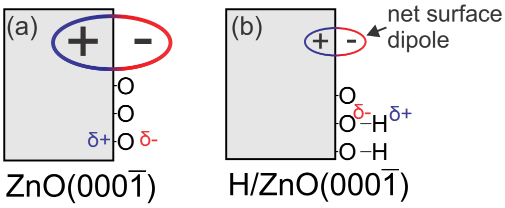

Figure 2.1.2: Modification of the surface dipole upon hydrogen adsorption on the ZnO(000$\bar{1}$) surface. Due to charge transfer, the net surface dipole is reduced.

2.1.2(a) simplified scheme of the oxygen terminated ZnO(000$\bar{1}$) surface is depicted. The high surface dipole originates from the distribution of partial charges between the surface O atoms and Zn atoms attached to the bulk material (gray shaded area).

Figure 2.1.2 depicts the H covered ZnO(000$\bar{1}$) surface. Here, adsorption of H on ZnO is accompanied by the formation of an OH bond at the surface. Due to the well-known polarity of this bond, with most electron density located at the O atom, the net surface dipole is gradually reduced upon H adsorption.

While in the case of H adsorption the H atom is directly attached to the surface O via a chemical bond, thus this process is called chemisorption, interface formation with other atoms or molecules often is achieved by physisorption, i.e. van-der-Waals and electrostatic interaction of surface and adsorbate. Also this process is governed by a redistribution of the charges at the surface and thus accompanied by a manipulation of the surface dipole. Moreover, adsorption with a permanent dipole moment can significantly alter the workfunction of a solid. However, such effects are out of the scope of this thesis.

2.2 Relaxation pathways of photoexcited electrons

Photoexcitation of a semiconductor typically leads to the creation of excited electrons in the conduction band (CB) and thereby leaving a positively charged hole in the valence band. These electrons and holes then relax to the band edges on ultrafast timescales (femtoseconds) by a variety of different processes belown, and can then form excited bound electron-hole pairs, i.e. excitons (see Section 2.3). The relaxation of the excited electrons occurs by dissipation of their excess energy. Typically this dissipation is determined by scattering processes with other (quasi-)particles. Predominantly, this scattering partners are other electrons and phonons.

Electron-elcectron scattering, in which the amount of dissipated energy can be relatively high, is commonly attributed to solid state materials with high charge carrier density, such as metals. In this process the excess energy of an electron in the CB can be transferred via collisions with low energy electrons below E_F, lifting them to higher energies. Note that both, energy and momentum have to be conserved in this process. Therefore, the electronic band structure strongly influences carrier lifetimes in metals.

In contrast to electron-electron scattering, the amount of energy dissipated per scattering event is usually relatively low for electron-phonon scattering, on the order of tens of meV. It is the most prominent relaxation mechanism for excess electrons in semiconductors. Due to the existence of the band gap and the resulting lower charge carrier density near E_F, the probability of scattering with electrons is reduced. However, the excess energy can be transferred to the lattice by excitation of phonons. Due to the small energy loss per scattering event, the amount of scattering events required is considerably higher. This, usually, enhances the lifetimes of excited electrons in semiconductors. However, in the case of strong electron-phonon coupling, in particular to high energy optical phonons. the lifetimes can still be on femtosecond time scales.

2.3 Excitons

The existence of excitons in direct band gap semiconductors is one of the key properties of these materials for possible application in optoelectronic devices such as LEDs of solar cells. But, what is an exciton?

In the simplest description ”an exciton is a quantum of electronic excitation energy traveling in the periodic structure of a crystal; it is electrically neutral and hence its movement through the crystal gives rise to the transportation of energy but not charge”[1]. To create a more physical picture; an exciton is a quasi-particle formed upon optical excitation of an electron from the valence band (VB) into the conduction band (CB). The thereby created charge vacancy in the VB, the positively charged hole, induces an attractive Coulomb interaction toward the electron in CB. Hence, they can form a bound pair state, similar to that of the hydrogen atom, with a finite binding energy and life time.

There are two distinct types of excitons, which are commonly observed. They mainly differ in their degree of localization and their binding energy with respect to CB:

- **Wannier-Mott excitons** are electron-hole $(e - h)$ pairs with a binding energy of a few tens of meV or lower. As this binding energy is a result of the $e - h$ Coulomb interaction $(-{}^{e^2}\!/\!{}_{\epsilon r})$, the low binding energy goes along with long $e - h$ distance r, which typically exceeds the lattice constance, i.e. a degree of delocalization. They usually appear in inorganic semiconductors.
- **Frenkel excitons** are strongly bound $e - h$ pairs with binding energies from 0.1 to 1 eV. They are generally found in weakly bound organic molecular crystals and their $e - h$ distance usually is comparable or less than the intermolecular distance. Hence, Frenkel excitons are strongly localized to single molecules in the solid.

As initially mentioned, these charge-neutral quasi-particles, which are a direct result of optical excitation, are able to move within the crystal lattice and thus transport excess energy, but not charge. This excess energy can be dissipated and gives rise to the following optoelectronic effects. Either excitons can be separated into free charge carriers by collision with another exciton or defect sites in the lattice, e.g. vacancies or foreign atoms. Charge separation can also happen at the interface to a different material, which acts as electron or hole acceptor. In this scenario, charge transfer is enabled leading to photoconductivity. On the other hand, a radiative decay channel is possible for the exciton, by $e-h$ recombination under emission of a photon, called photoluminescence.

So far, these properties apply for the exciton as a non-interacting excited quasi-particle with a large distance between neighboring excitons. However, one can imagine that for high number of $e-h$ pairs the distance reduces and an interaction sets in. This interation is mostly determined by the Coulomb interaction between the charged particles and manifests itself by redistribution of charges, resulting in a screening effect.

In the experiment, the number of $e-h$ pairs is proportional to the excitation density. Hence, for very high excitation densities, the density of $e-h$ pairs is increased until the inter-exciton distance d is lower than the exciton radius r_{exc}. This scenario is schematically depicted in Figure 2.3.1.

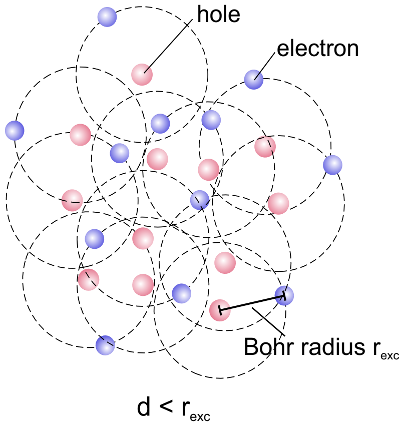

Figure 2.3.1: Electron hole plasma formation for excitation densities above the Mott limit (image in courtesy of J.-C. Deinert).

Here, the collective state of electrons (blue spheres) and holes (red spheres) is shown with $d < r_{\mathrm{exc}}$. In this state the Coulomb interaction of electrons in the CB and holes in the VB is screened and the $e-h$ pairs can no longer be described as excitons, instead the collective state is denoted as a conductive electron-hole plasma (EHP). The required charge densities, respectively the excitation density to generate the EHP in a semiconductor is described as the Mott density or Mott limit. In the literature, the values for the Mott density spread from 1.5 to 6×10^{18} cm^{-3} for ZnO [2, 3, 4].

2.4 Structure and ultrafast dynamics of Zinc oxide surfaces

Zinc oxide (ZnO) is a widely used material with a variety of applications in different fields. Most often to be seen in everyday life it is applied as pigment, as so called zinc white, in painting and coloring of e.g., paper. Due to its antiseptic properties zinc oxide is also used in medical or pharmaceutical applications [5]. Like other metal oxides it is employed in chemical processes as a heterogeneous catalyst e.g., during the industrial pruduction of methanol or the vulcanisation of rubber [6]. In addition to these already widely spread ranges of use, ZnO has attracted considerable amount of attention in the past couple of years based on its special electronic and optical properties. As a wide band gap semiconductor, it is transparent for visible and near ultraviolet light and is included in a new class of materials called ‘transparent conducting oxides (TCO)’. Thus, it is an attractive material for the application as transparent electrode in organic/inorganic solar cells [7].

Bulk zinc oxide is a II^b-VI compound semiconductor with a wide direct band gap of 3.37 eV [8, 9, 10, 11] mainly crystallizing in a hexagonal wurtzite fashion with point group $6mm$ (C_{6v}), space group P6$_3$mc and the lattice parameters a = 3.25 Å and c = 5.206 Å [12, 11, 10]. In addition to the wurtzite structure, a cubic zincblende structure can be observed when ZnO is grown on a cubic host lattice [13]. In both cases, each Zn^{2+} cation is surrounded by a tetrahedron of O^{2-} and vice versa. Under rather rough conditions e.g., pressure in the region of GPa, zinc oxide is present in a rock salt structure [13]. Nevertheless under most conditions the wurtzite structure is the thermodynamically most stable one [10]. Regarding an ideal crystal its periodicity is infinitely expanded. But when considering a real crystal within finite dimensions, consequently different surfaces with respect to different directions in the periodic crystal lattice emerge. Obviously, these surfaces lead to a break in symmetry in one direction, therefore the band structure changes in comparison to the bulk. Since a high number of applications is connected to interactions between the surface and its environment e.g., molecules in heterogeous catalysis, an insight into the atomic and electronic surface structure is necessary. Concerning the atomic structure various studies of the low index surfaces of ZnO have been performed using several surface sensitive techniques like low energy electron diffraction (LEED), low energy ion scattering (LEIS), scanning tunneling miscroscopy (STM) and grazing incidence x-ray photoemission spectroscopy (GIXPS) [5, 14, 15].

Of highest interest are the four low index surfaces: the polar (0001)-Zn and (000$\bar{1}$)-O terminated, and the nonpolar (10$\bar{1}$0) and (11$\bar{2}$0) surfaces. The term ‘polar’ mentioned for ZnO(0001)-Zn and ZnO(000$\bar{1}$)-O refers to the projection of the bulk dipole moment on the surface normal. This projection is different from zero for ionic single crystals with a non-centrosymmetric point group – C_{6v} has no inversion center – therefore yielding an electrostatic field which needs to be compensated to stabilize the respective surface [5]. While polar surfaces should usually be unstable due to compensation mechanisms e.g., reconstruction (thereby the surface geometry would be changed), these two polar surfaces of ZnO are surprisingly stable [5].

ZnO(0001)-Zn, as the indexing suggests is Zn-terminated and exhibits a relatively rough surface morphology characterized by (1 x 1) terraces highly stepped with triangular pits and islands. The high density of O-terminated step-edges decreases the overall Zn surface concentration and compensates for the surface polarity [16].

In contrast, the O-terminated polar (000$\bar{1}$) surface shows a different morphology of relatively smooth hexagonal terraces with a considerably low step density [15]. Additionally, there are theoretical and experimental results suggesting a relaxation of the outermost Zn-O double layer [17]. Regarding the surface termination, it is still under debate whether the commonly observed bulk-like hexagonal (1 x 1) pattern really reflects the structure of the clean surface or is a result of H adsorption and the clean surface should exhibit a (1 x 3) reconstruction instead to compensate the polarity [18].

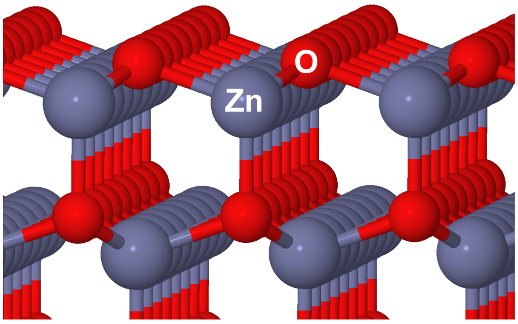

Figure 2.4.1: Structure of the ZnO($10\bar{1}0$) surface (image in courtesy of B. Bieniek)

The ZnO($11\bar{2}0$) surface contains an equal number of zinc and oxygen ions per unit area and therefore belongs to the nonpolar surfaces. According to calculations [19] it is the most unstable of the mentioned low-index surfaces with the highest surface energy which is represented by a rough morphology mainly consisting of deep grooves.

In comparison with the previous mentioned surfaces, ZnO($10\bar{1}0$) is the one with lowest surface energy, hence the most stable one. Like the ($11\bar{2}0$) surface, it is mixed-terminated with zinc and oxide ions in equal stoichiometry resulting in a dipole moment equal to zero. In STM images, a wide-stretched rectangular terrace structure with a small number of defects can be seen. As depicted in Figure 2.4.2, the surface is formed by dimer rows of Zn and O atoms without any hint of surface reconstruction nor relaxation, hence ZnO($10\bar{1}0$) is said to be similar to a truncation. Based on the remarkable stability accompanied by the well-ordered structures, the O-terminated polar ($000\bar{1}$) and the nonpolar ($10\bar{1}0$) surface have been investigated within the context of this work.

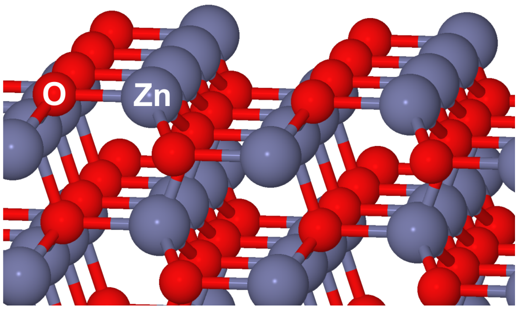

Figure 2.4.2: Structure of the ZnO($10\bar{1}0$) surface (image in courtesy of B. Bieniek)

Concerning the electronic structure of both surfaces emerging from the same bulk material, their valence electronic structure is composed of hybridized Zn $4sp$-O $2p$ valence bands (VB) with O $2p$ being the dominating contribution at the valence band maximum (VBM) and the mainly Zn $4s$-based conduction band (CB) which are separated by a bulk energy gap of 3.4 eV. However, when regarding the clean surfaces some differences can be spotted. In photoemission studies by Ozawa and Mase [20] the VBM of ($10\bar{1}0$) and ($000\bar{1}$) could be observed 3.3 and 2.9 eV binding energy respectively. This is associated with a slight downward band bending for the nonpolar and a slight upward bending for the polar surface. This situation is schematically depicted in Figure 2.4.3.

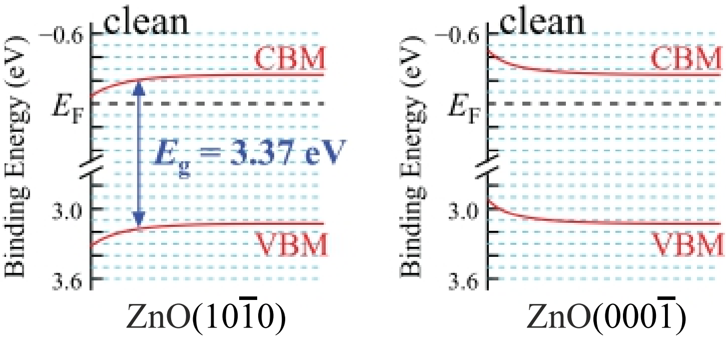

Figure 2.4.3: Energy diagram of the ZnO(10$\bar{1}$0) (left) and ZnO(000$\bar{1}$) (right) valence electronic structure from Ref. [20]

But upon exposure to electron donating adsorbates, e.g. atomic hydrogen or small molecules such as methanol and water, both surfaces exhibit the same behavior. Valence band photoemission spectra of H covered (10$\bar{1}$0) and (000$\bar{1}$) surfaces reveal a feature within the band gap directly at the Fermi energy E_F. This feature is associated with a downward band bending of the CB below E_F resulting in additional occupied density of state (DOS) [20]. This effect is schematically depicted in a quite demonstrative manner in Figure 2.4.4 by Ozawa and Mase [21] for the H adsorption on the nonpolar (10$\bar{1}$0) surface.

The left part of Figure 2.4.4 again shows the initial situation of a clean surface with the VB of Zn 4sp-O 2p and CB of Zn 4s character separated by bulk band gap which are slightly bent downward, thereby the CBM nearly crosses E_F. The right panel shows the

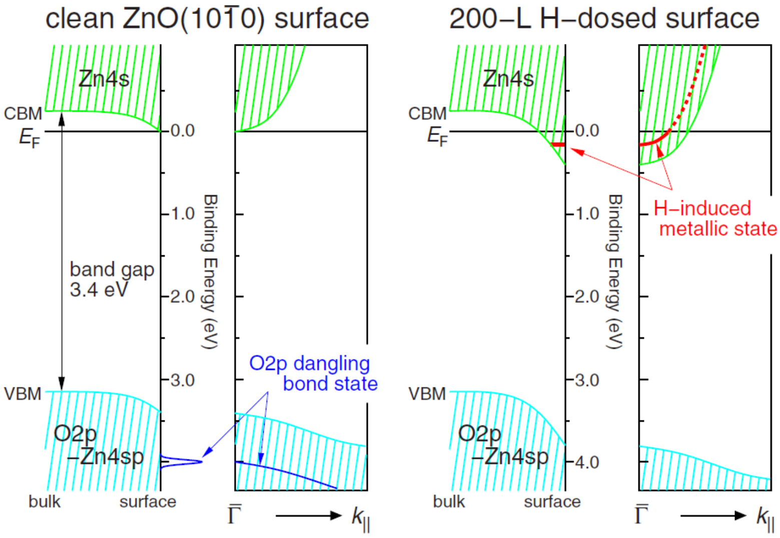

Figure 2.4.4: (left) Scheme of the electronic band structure of clean ZnO(10$\bar{1}$0) (right) hydrogen induced metallization of ZnO(10$\bar{1}$0) [21]

nonpolar surface after exposure to 200 L H. Here, the band bending is increased such that the CBM is shifted to 0.40 eV below E_F. Atomic hydrogen binding to the O sites on the mixed-terminated surface donates charge into the surface layer, which is therefore often refered to as a charge accumulation layer (CAL) [22], thus partially populates a shallow subband up to E_F within the bent conduction band. Using angle-resolved photoemission spectroscopy (ARPES) Ozawa et. al. investigated the dispersion of this subband. They extract a symmetrically parabolic dispersion in the two orthogonal directions of the rectangular surface brillouin zone (SBZ), i.e. a metallic character of this surface bands. The isotropic dispersion within the rather anisotropic SBZ is explained by major contribution of highly extended atomic orbitals which is in agreement with the suggested Zn4s character of the ZnO conduction band. Regarding the isotropy of the hydrogen-induced CAL on ZnO($10\bar{1}0$), they conclude that the CAL can be denoted as two-dimensional electron gas [23].

Since the appearance of the CAL on the ZnO surface is a result of charge transfer from adsorbed H to O-sites, it is plausible to find the same behavior for the O-polar ($000\bar{1}$) surface as also observed in Ref. [20]. While most studies of the semiconductor-to-metal transition on ZnO are focused on highly H covered surfaces, recently Deinert et al. studied the build-up of the CAL on the nonpolar ZnO($10\bar{1}0$) surface to get a detailed understanding of the ZnO-H interaction, since H is ubiquitous at least in small amounts under UHV conditions as well as under industrial conditions [24, 25]. Some of his results are depicted in Figure 2.4.5. There, the photoemission signal of the CAL, directly below E_F, is shown

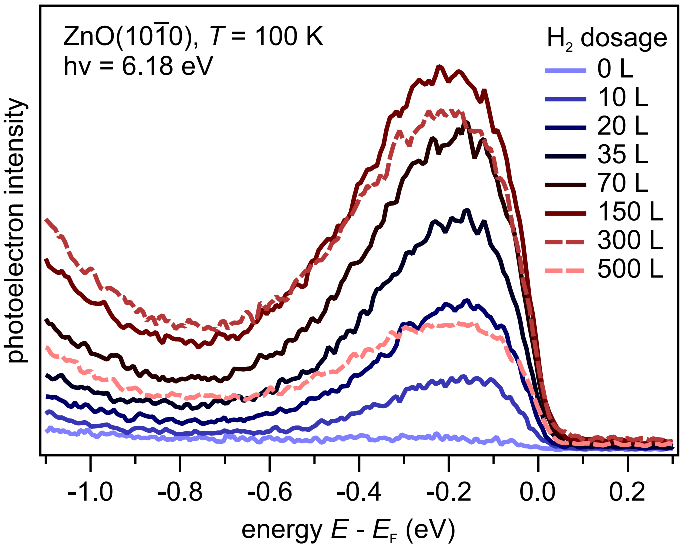

Figure 2.4.5: Buildup of the photoemission signal of the CAL on ZnO($000\bar{1}$).

for an increasing H dosage, from the pristine to a highly covered surface with 500 L. As one can clearly see, the CAL intensity drastically rises with increasing H coverage and subsequently decreases again.

This behavior is also reflected in Figure 2.4.6, where the CAL intensity (blue curve) is plotted as a function of the H dosage in L. The CAL formation is, furthermore, accompa-

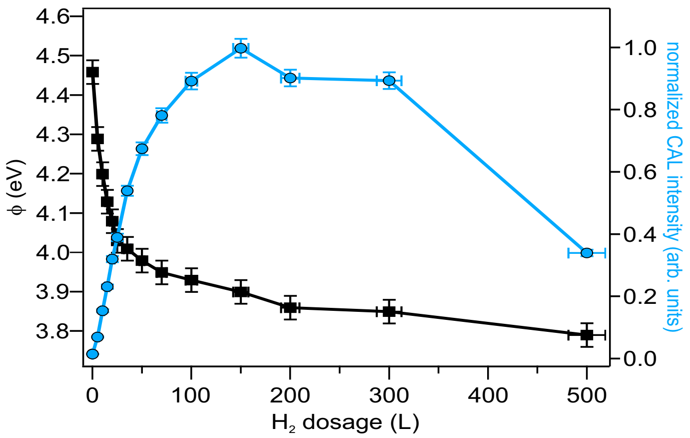

Figure 2.4.6: Workfunction Φ and normalized CAL intensity on ZnO(000$\bar{1}$) as a function of the H dosage.

nied by a drastic shift of the workfunction Φ (black curve) from initially 4.50(5) eV on the pristine surface to 3.85(5) eV, which indicates a distinct lowering of the surface potential by lowering the surface dipole by H adsorption on the O-sites.

Apart from the donor-induced formation of metallic states at the semiconductor's surface, ZnO exhibits some very interesting ultrafast dynamics upon exposure to UV light. These dynamics are briefly shown in the time-resolved two-photonphotoelectron spectra (tr-2PPE) in Figure 2.4.7 (This technique is described in Section3.1 in more detail). In

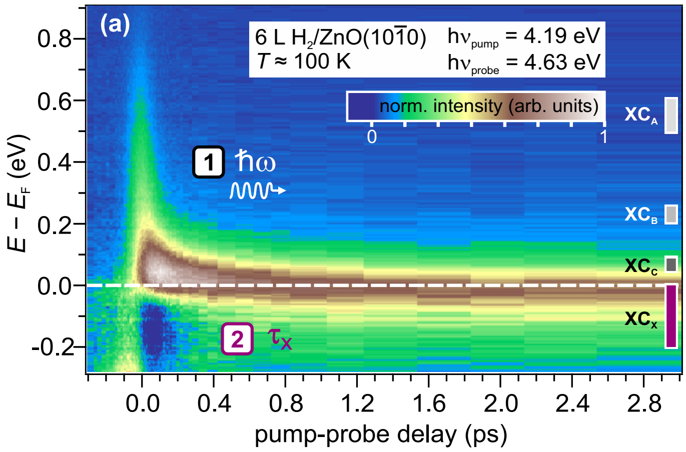

Figure 2.4.7: 2D plot of the photoinduced ultrafast electron dynamics above E_F and SX formation below E_F from Ref. [24].

this experiment, the system is excited from its equilibrium state by a first laser pulse (hν = 4.2 eV) and subsequently a second laser pulse (hν = 4.6 eV) is used to protbe the resulting non-equilibrium dynamics by photoemission. The time resolution is achieved by a time delay between the two laser pulses. Figure 2.4.7 displays a two-dimensional PE spectrum of the H/ZnO(10$\bar{1}$0) surface with PE intensity in false colors as a function of pump-probe delay and energy with respect to E_F. The equilibrium background was substracted, i.e. the intensity shown here is solely resulting from the electrons excited from the VB above the band gap of 3.4 eV into the CB. As one can clearly see, this excitation enables the observation of a broad energy distribution around zero time delay, associated with ultrafast fs dynamics, and followed by a narrow long-lived signal which extends to several hundreds of ps.

The ultrafast dynamics exhibits a fast time constant τ = 20 - 40 fs for high energies, which points toward a very effective decay mechanism of the excited electrons [24]. It was pointed out in Section 2.2 that the relaxation rates and relaxation times of excited electrons in semiconductors are dominated by scattering processes with lattice phonons. The theoretical work by Zhukov et al., which focuses on the dynamics of excited electrons in the CB of bulk ZnO, attributes these ultrafast dynamics to the scattering with longitudinal optical phonons [26].

A possible contribution of acoustic phonons to the electron-phonon scattering can be detected by temperature-dependent measurements. With their low energies, compatible with thermal excitations ($k_{\mathrm{B}}T_{\mathrm{rt}} = 25$ 0eV), the occupation distribution of acoustic phonons depends strongly on the temperature. However, the relaxation times of CB electrons at the ZnO($10\bar{1}0$) surface do not exhibit a temperature dependence [24]. Hence, the ultrafast dynamics on ZnO($10\bar{1}0$) were, in agreement with Ref. [26], assigned to scattering with optical phonons.

The slower dynamics of the long-lived state in Figure 2.4.7 are accompanied by a shift of the peak below E_{F}. As E_{F} marks the energy of the highest occupied state in equilibrium the observation of additional PE intensity/DOS seemed to be counterintuitive. Increased PE intensity below E_{F} must be related to the creation of additional states by photoexcitation. There are three scenarios possible to explain this observation: (i) the formation of small polarons, a quasiparticle consisting of an electron/hole screened by the surrounding atoms, (ii) photoinduced changes of the surface electronic structure, e.g. surface photovoltage effects or heating or (iii) the formation of an exciton.

While the formation of small polarons (i) could be ruled out by time-resolved THz spectrocopy [2], the experimental differentiation between (ii) and (iii) was performed by varying the excitation density (A more detailed description of this experiment follows in Section 4.2). This experiment showed that the additional PE intensity below E_{F} can be assigned to the formation of a surface excitonic species (SX). It was also concluded that SX is promoted by the donor-induced downward band bending below E_{F} at the ZnO($10\bar{1}0$) surface. Due to its high stability (ns) even at room temperature, the SX represents an ideal candidate for energy transfer applications.

Since, the existence of the CAL induced by surface downward band bending plays a major role for the ultrafast formation of the remarkably stable excitonic species at the nonpolar ZnO($10\bar{1}0$) surface, this work investigates the polar ZnO($000\bar{1}$) surface with particular focus on the comparison of both surfaces' behavior toward H adsorption and CAL formation as well as photoinduced exciton formation dynamics.

2.5 SP6

Since, the long-term motivation is the combination of organic and inorganic materials in optoelectronic and photovoltaic devices, the interface formation of the previously mentioned ZnO surface with possible optically active organic molecules needs to be studied. Among the variety of candidates, the spirobifluorene derivative 2,7-bis(biphenyl-4-yl-)2',7'-ditertbutyl-9,9'-spirobifluorene (SP6) shown in Figure 2.5.1 is a promising molecule: SP6 is an organic semiconductor with a wide HOMO/LUMO gap $\Delta E_{\mathrm{g}}^{\mathrm{HOMO/LUMO}}$ of 3.6 eV and a high photo- and thermal stability.

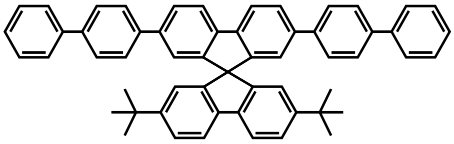

Figure 2.5.1: Lewis structure of the SP6 molecule.

Earlier studies on solid SP6 have shown a lasing effect which may allow for the fabrication of organic condensed state lasers tunable from blue to near UV light (2.8 - 3.1 eV)[27]. Furthermore, it exhibits a Frenkel-type exciton with a binding energy of 0.45 eV[28]. First investigations of SP6 on the polar ZnO(000$\bar{1}$) surface were presented in Ref.[29] and [30] using atomic force microscopy (AFM), photoemission (PE) and photoluminescence (PL) spectroscopy. SP6 shows a homogenous growth of closed amorphous layers, due to the spiro linkage of the fluorene units. The energy level alignment is of the staggered "type II"[31], which means that HOMO and LUMO are positioned at higher energies than the VBM and the CBM, and no indication of band bending of the ZnO bands or shifts of the SP6 energy levels were detected for differing layer thickness [29]. In correlation with the Raman study by Stähler et al.[32] the interaction of SP6 with the ZnO surface could be attributed to physisorption via van-der-Waals interactions [29]. Moreover, the type II alignment enables the charge separation of the Frenkel exciton at the interface.

A recent study by Foglia et al. used time-resolved optical spectroscopy to investigate excited state dynamics in a SP6/ZnO(10$\bar{1}$0) hybrid system [33]. An overview of the results is shown in Figure 2.5.2, by a scheme of the molecular electronic states, including vibrational levels. Above gap excitation leads to the population of vibrationally excited states in the singlet S_1. Probing the excited state absorption (ESA) into S_n states at varying time delay revealed relaxation times of 2 - 9 ps for the intramolecular vibrational relaxation (IVR) into the S_1 vibrational ground state with a lifetime of 200 - 300 ps ($S_1 \rightarrow S_0$). Furthermore, a long-lived dark state (DS) is observed, exceeding lifetimes of several µs, which is formed by intersystem crossing (ISC).

However, as transient optical spectroscopy is sensitve to electronic resonances only, crucial information on the absolute energy level alignment is still missing. This can be provided by photoelectron spectroscopy and will be discussed in Section 5.

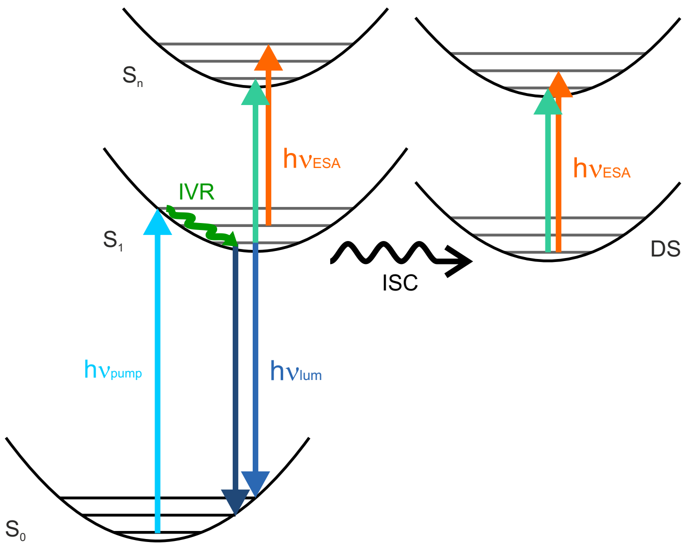

Figure 2.5.2: Energy levels and dynamics of SP6 from time-resolved optical measurements (image in courtesy of L. Foglia [33]).

3 Experimental

3.1 Photoelectron Spectroscopy

Photoelectron spectroscopy (also photoemission spectroscopy) generally abbreviated as PES is a widely used technique for the investigation of the electronic structure of atoms and molecules in different aggregate states, i.e. solid, gaseous or liquid [34]. The elementary process of this method is based on the photoelectric effect [35]: A material irradiated by photons with an energy $E_{\text{photon}} = h\nu$, with h being the Planck constant and ν the frequency of impinging light, emits electrons with a defined kinetic energy E_{kin} if the following equation is satisfied:

$$E_{\text{kin}} = h\nu - \Phi + E_{\text{b}} \tag{3.1.1}$$

The workfunction Φ of the material is defined as energy difference between vacuum energy E_{vac} and Fermi energy E_{vac}

$$\Phi = E_{\text{vac}} - E_{\text{F}}. \tag{3.1.2}$$

E_{b} is the binding energy of electrons with respect to the Fermi energy. As the escape depth of emitted electrons in condensed matter is limited by scattering processes, the technique is very surface sensitive, making PES a standard technique for surface sciences. The resulting PE spectrum is usually displayed as an energy distribution curve which is often interpreted as a projection of a material's occupied density of states (DOS) as it is schematically depicted in Figure 3.1.1. Here, a metal's DOS *N(E)* is displayed in an energy diagram and absorption of photons $h\nu$ gives the electron distribution curve $I(E_{\text{kin}})$. Depending on the photon energies used for electron excitation into the vacuum one can access different energy levels. For example by using UV light (3 – 100 eV) for photoemission – referred to as UPS – information on the rather broad valence band states up to the Fermi energy E_{F} is accessible. Application of higher energetic photons in the X-ray regime ($h\nu \geq 100$ eV; XPS) enables emission from the narrow core levels. However, by using the mentioned techniques only information about occupied states is accessible.

The study of unoccupied states is either possible by *inverse photoemission spectroscopy* (IPES) or by *two-photon photoelectron spectroscopy* (2PPE). In the former method, an electron beam of defined kinetic energy impinges on the samples surface to populate unoc-

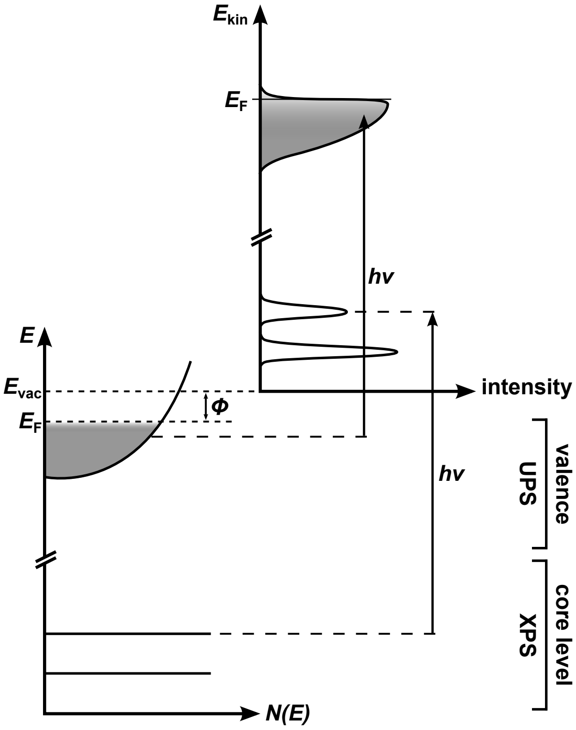

Figure 3.1.1: Energy diagram and schematic photoelectron spectrum

cupied states. Subsequently, photons resulting from the radiative decays into lower lying unoccupied states can be detected. Whereas in 2PPE a pulsed light source with high photon density is used to enable a stepwise excitation process. Thereby, the first photon $h\nu_{\text{pump}}$ excites an electron from an occupied state below E_{F} into an unoccupied intermediate state above E_{F} (see Figure 3.1.2). Subsequently, the electron is emitted by the second photon $h\nu_{\text{probe}}$. 2PPE can be performed as one-color ($h\nu_{\text{pump}} = h\nu_{\text{probe}}$) or as two-color experiment ($h\nu_{\text{pump}} \neq h\nu_{\text{probe}}$). As the intensity of the 1PPE process (direct photoemission) is by far more pronounced than for 2PPE, one should take care that $\sum_{i=1}^{2} h\nu_i < \Phi$ holds.

There are several pathways for the stepwise excitation of an electron from its initial state below E_F passing through an intermediate state below E_{vac} till it reaches its final state above E_{vac}. These mentioned mechanistic pathways are depicted in the following Figure 3.1.2.

a) **Resonant excitation** occurs when the photon energy $h\nu_{\text{pump}}$ matches precisely the energy difference between the initial state E_i and a real intermediate state E_x ($h\nu_{pump} = E_x - E_i$).

b) The excitation process may take place in an **indirect** way, too. In this case an electron gets excited above a real intermediate state E_x and reaches it by an energy loss via inelastic scattering processes e.g. electron-electron or electron-phonon scattering.

c) When there is no real intermediate state available, the photoelectron is emitted non-

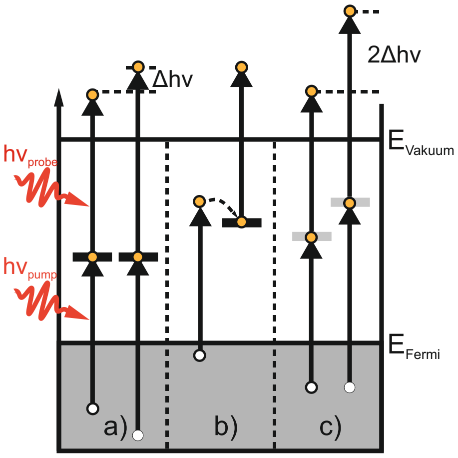

Figure 3.1.2: Excitation mechanisms for the 2PPE process (modified from [36])

resonantly via a virtual intermediate state E_{virtual}. The emission of the electron in this case can be visualised by simultaneous absorption of the two photons $h\nu_{\text{pump}}$ and $h\nu_{\text{probe}}$.

As the occupied initial states lying below E_{F} are used to populate the unoccupied states above E_{F} with the stepwise excitation process, 2PPE provides the possibility to observe occupied and unoccupied states simultaniously. A distinction can be achieved considering the three different excitation mechanisms. Apparently, excitation via a virtual intermediate state as depicted in Figure 3.1.2c) leads to the emission of electrons originating from initial states below E_{F}. Thus a change in the photon energy $\Delta h\nu$ (considering a one-color 2PPE experiment) would result in a photoelectron signal shifted by $2\Delta h\nu$ as the process is associated with absorption of two photons simultanously. A shift by $1\Delta h\nu$ can be related to emission from a real intermediate state E_{x} (see Figure 3.1.1a)). Once E_{x} is populated, the final state energy of the emitted electron only depends on $h\nu_{\text{probe}}$. Certainly, in two-color 2PPE, the complexity increases due to the possibility to populate different intermediate states. However, spectral interpretation can be done by successively changing photon energies and following the peak maxima versus the photon energies. The thereby obtained slopes provide information about the origin of the emitted electrons.
Apart from the states observed in 2PPE- or PE spectra, there are two other basic features, a low and a high energy cut-off. The schematic overview in Figure 3.1.3 displays the origin of these cut-offs. For a simple understanding, these features are shown for the 2PPE-process at a metal surface. The low energy cut-off is also referred to as secondary edge, whereas the one at higher energies is called Fermi edge. Electrons at the latter position have the highest possible kinetic energy ($E_{\text{F}}^{kin} = h\nu_{\text{pump}} + h\nu_{\text{probe}} - \phi$). They originate from occupied states directly at the Fermi level, and one can therefore only expect to see this high energy cut-off when the investigated system has occupied states at its Fermi level as it is the case for metals. The secondary edge results from electrons with an energy

just sufficient just to overcome the workfunction Φ. Hence, they have the lowest possible kinetic energy ($E_{\mathrm{SE}}^{\mathrm{kin}} = 0$) and basically provide less information about the electronic structure itself but about the width of the spectra $\Delta E_{\mathrm{kin}} = E_{\mathrm{F}}^{\mathrm{kin}} - E_{\mathrm{SE}}^{\mathrm{kin}}$ and therefore about the workfunction.

$$\Phi = (h\nu_{\mathrm{pump}} + h\nu_{\mathrm{probe}}) - \Delta E_{\mathrm{kin}} \tag{3.1.3}$$

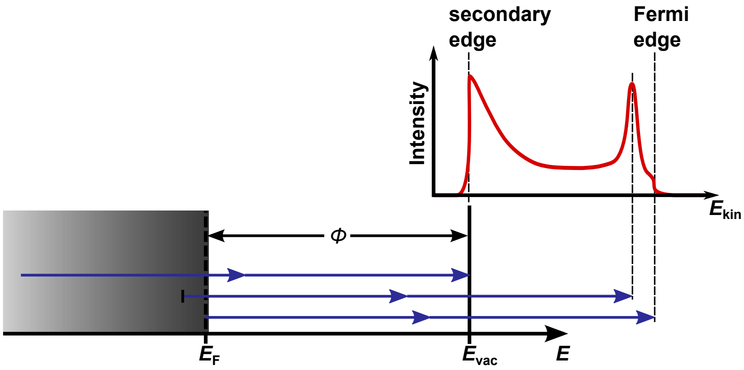

Figure 3.1.3: Schematic overview of basic features in the 2PPE spectrum

In addition to the accessibility of unoccupied states, 2PPE offers the opportunity to investigate electron population dynamics of these excited states e.g., lifetimes or a time-dependent binding energy shift, which usually proceed on femto- and picosecond timescales. The general picture of time-resolved two-photon-photoemission (TR-2PPE) is shown in the following Figure 3.1.4. In this scheme, $h\nu_{pump}$ induces a non-equilibrium state of the system, while $h\nu_{probe}$ monitors the resulting dynamics through photoemission. The time resolution is achieved by controlled variation of the time delay Δt between the pulses $h\nu_{pump}$ and $h\nu_{probe}$ when ultrashort laser pulses with pulse durations below 100 fs are applied. Experimentally this is realized by changing the optical path length of one beam via a delay stage while the other path remains unaltered. Moving the stage provides the possibility of increasing or decreasing the path length and thereby adjusting Δt.

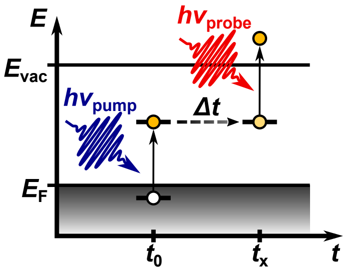

Figure 3.1.4: Principle of time-resolved 2PPE spectroscopy

3.2 UHV Chamber

2PPE requires ultra high vacuum (UHV) conditions in order to minimize the possibility of collisions of emitted electrons with residual gas molecules and to have a clean sample for as long as possible. The collision possibility is usually described by means of kinetic gas theory with the mean free path which is in the range of 10^6 m at a pressure of 10^{-9} mbar or lower. Under these conditions the purity of the sample surface, which strongly affects its electronic structure, can be ensured for a longer time.

The UHV chamber illustrated in Figure 3.2.1 consists of two vertically aligned compartments. The left side of Figure 3.2.1 shows the upper part, the so-called preperation chamber whereas the lower part, the spectrometer chamber, is shown on the right-hand side. Both levels can be separated by a gate valve to avoid contamination of the analyser region during sample preparation. The sample (ZnO single crystal with a $(000\bar{1})$ surface) is mounted on a manipulator and can therefore be moved through both levels of the chamber in four dimensions – x-, y-, z-direction and rotation around the z-axis about the angle ϕ. The ZnO crystal is clamped on a tantalum sheet fixed to the lower part of a sample holder via tantalum wires. It can be indirectly cooled by taking advantage of the thermal conductivity of the sample holder that is connected with a cryostat which can be operated with either liquid nitrogen (N_2) or liquid helium (He). Temperature control of the sample is achieved by PID controlled resistive heating of the previously mentioned tantalum wires.

The upper chamber contains various tools for preparation and characterisation of different samples which can be transferred into the chamber without braking the vacuum using a separately pumped transfer system. In the course of this work, sample preparation is mainly done by using the sputter gun, the resistive heating of the sample and the leak valve connected to a nearby gas sytem. For the preparation of organic adsorbate layers a Knudsen cell can be used. The layer thickness can be charactarized by using a Quartz microbalance (QMB) and/or thermal desorption measurements with the quadrupol mass spectrometer.

The spectrometer chamber mainly consists of a hemispherical analyzer (Phoibos), two windows for the entrance and exit of the laser beam. The inner wall of the spectrometer chamber is surrounded by a μ-metal shielding to minimize the influence of an outer magnetic field on the trajectories of photoelectrons.

3.3 Laser system

For the generation of ultrashort laser pulses of different wavelengths a commercially available laser system (*Coherent*) is used. This arrangement is placed in a tent with flow boxes on the ceiling which provide a slight overpressure to minimze the deposition of dust on the optics. To ensure optimal operational capability, the temperature and humidity in

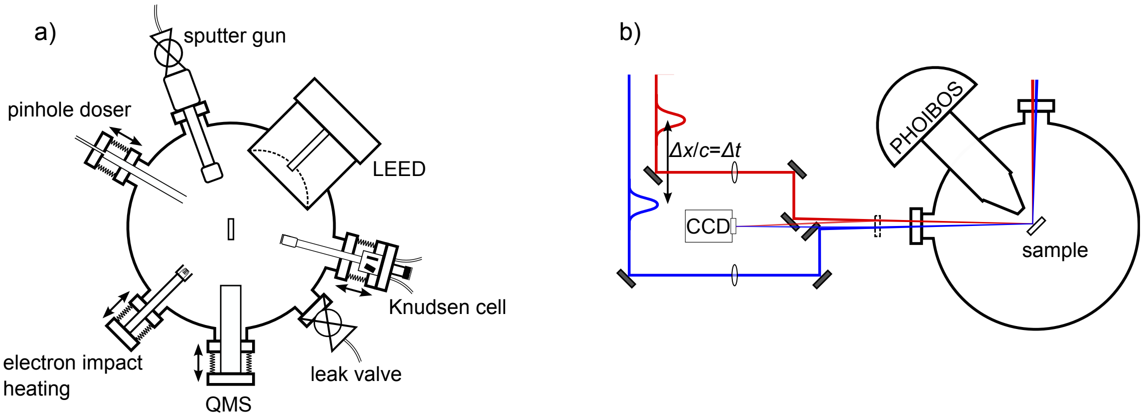

Figure 3.2.1: UHV chamber consisting of two levels a)preparation chamber (top) b) spectrometer chamber (bottom; modified from [37])

the whole laboratory is kept constant. The laser system schematically shown in Figure 3.3.1 consists of the pump laser (*Verdi G18*), a titanium-sapphire oscillator (*Vitara*), a regenerative amplifier (*RegA 9050*), a *Stretcher/Compressor* unit and an optical parametric amplifier (*OPA 9450*). The *Verdi G18* is a diode pumped solid state laser which provides cw radiation of 532 nm with a maximum beam power of 18 W. Its output is split and on the one hand used for pumping the *Vitara*, which yields ultrashort laser pulses of 800 nm (1.55 eV photon energy) with a pulse energy of 4 nJ. On the other hand the *Verdi* output is used to amplify the stretched 800 nm pulses. After passing the *Compressor*, the pulse length is in the range of 40 fs with a pulse energy of 2.7 μJ and a repetition rate of 200 kHz. This beam is split and the one part is coupled into the *OPA* to convert it into light of 480 - 700 nm (1.77 - 2.58 eV) by using non-linear optical effects. The other remaining 800 nm can directly be used for the experiment or converted into 400, 266 or 200 nm light (3.1 , 4.6 or 6.2 eV) by nonlinear processes like second harmonic generation (SHG) and sum frequency generartion (SFG), which are discussed elsewhere [37].

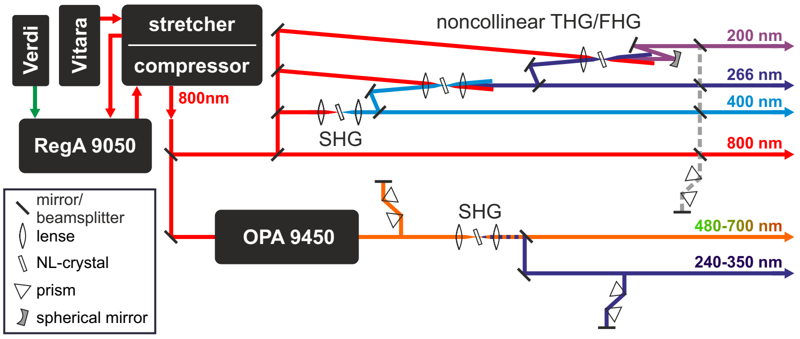

Figure 3.3.1: Schematic overview of the tunable fs laser system(image in courtesy of J.-C. Deinert and D. Wegkamp)

4 Electronic structure & ultrafast dynamics at ZnO surfaces

4.1 Hydrogen adsorption on ZnO($000\bar{1}$): Transition from upward to downward suface band bending

The hydrothermally grown ZnO($000\bar{1}$) single crystal sample (7 x 7 x 0.4 mm^3, MaTeck GmbH) was prepared by cycles of Ar$^+$ sputtering (1.0 keV, 0.6 µA, 10 min) and annealing at 950 K for 30 min under O_2 atmosphere (1 x 10^{-6} mbar) with heating rates of 30 K min^{-1}. Compared to the largely varying recipes in the literature **??** this preparation is relatively mild and straightforward. During all experiments, the base pressure was in the range of 10^{-10} mbar. The preparation cycles were repeated on a daily basis in order to maintain a well reproducible sample surface, which was characterized by PE measurements and LEED images. All LEED images of the freshly prepared as well as the H covered surface showed a (1 x 1) diffraction pattern of the hexagonal surface. As an example, Figure 4.1.1 shows a LEED image of the ZnO($000\bar{1}$) surface covered with 200 L H, which is basically identical to our observations of the freshly prepared surface (not shown). For a detailed description of the H dosing process see Section 4.1 below.

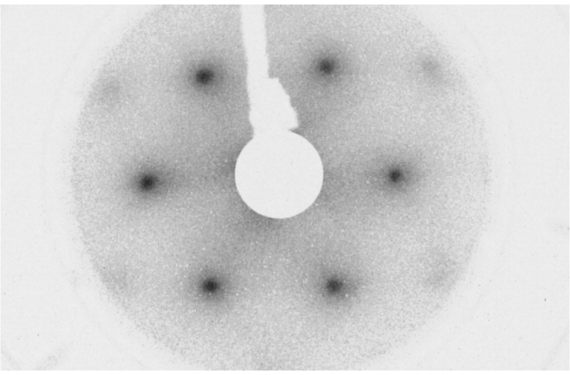

Figure 4.1.1: LEED image ($E_{\mathrm{kin}} = 94$ eV) of the H covered ZnO($000\bar{1}$) surface showing a (1 x 1) pattern, analogously to the freshly prepared surface (not shown).

For further sample characterization, we investigated the electronic properties of the clean surface by 2PPE. As explained in section 3.1, the secondary cut-off of the PE spectra can be used to determine the workfunction of the sample if the spectra are plotted as a function of the final state energy with respect to E_F. Figure 4.1.2(a) depicts a spectrum taken with $h\nu = 4.69$ eV as a function of the final state energy (bottom). The workfunction of the surface was determined to be 5.15(5) eV[1], which is agreeing with the literature value [20]. The energy diagram in Figure 4.1.2(b) shows that with $h\nu = 4.69$ eV a two photon process ($h\nu < \phi$) is required to emit electrons from the VB. The binding energy can be directly read from the initial state axis (top). Here, blue indicates the 2PPE signal and the red curve is a biexponential fit which is applied for subtraction of the secondary electron background. The respective background corrected signal of the VBM (blue) is depicted in the inset. By linear extrapolation (dark green) of the leading edge of the signal to the baseline the VBM is determined to be 2.99 eV below E_F.

It should be noted that the 2PPE spectra change with time after sample preparation. This is due to residual hydrogen in the rest gas spectrum, which immediatly binds to the surface and modifies its electronic structure. For comparison, the inset also shows the 2PPE signal for the $(000\bar{1})$ surface directly after the surface preparation (light blue) with its respective VBM (green). In this case the workfunction amounts to 5.2 eV and the onset of the VBM is located at 2.78 eV below E_F. In other words, both workfunction and VBM have shifted to lower energies by 100 meV due to residual gas adsorption.

In the case of downward surface band bending of 1 nm depth as for ZnO$(10\bar{1}0)$, the photoemission integrates over the whole downward bend VB and the maximum energy measured refers to the bulk VBM. Further hydrogen adsorption does not alter the spectrum. This is different when considering upward surface band bending for ZnO$(000\bar{1})$ as observed in previous studies [20]. Hydrogen adsorption leads to a lowering of the surface potential, thus reducing the upward surface band bending as illustrated in Figure 4.1.2(b). Photoemission probes the change of the VBM *at the surface* as observed ZnO$(000\bar{1})$ in Figure 4.1.2(a, inset). Based on these considerations, it can be concluded that the pristine ZnO$(000\bar{1})$ surface exhibits an upward surface band bending, which is inverted by hydrogen adsorption.

In a next step, the polar ZnO$(000\bar{1})$ surface was exposed to hydrogen in a controlled manner in order to characterize and quantify its impact on the electronic structure. Therefore, the sample was exposed to gradually increasing dosages of H. As schematically depicted in Figure 4.1.3(b), the H dosing was performed by backfilling of the UHV chamber with molecular H_2 at a constant background pressure of 2.2 x 10^{-7} mbar to give an estimation of the dosage in L (1L = 1.33 x 10^{-6} mbar s) at a constant dosing rate. The tungsten filament of the ion gauge (approx. 15 cm away from the sample surface) ensured the cracking of significant amount of molecular to atomic H, while the sample was held at 100 K.

---

[1] $\Phi = 5.1$eV is the value of the workfunction which was typically achieved whithin the daily lab routine, which is in good agreement with the literature.

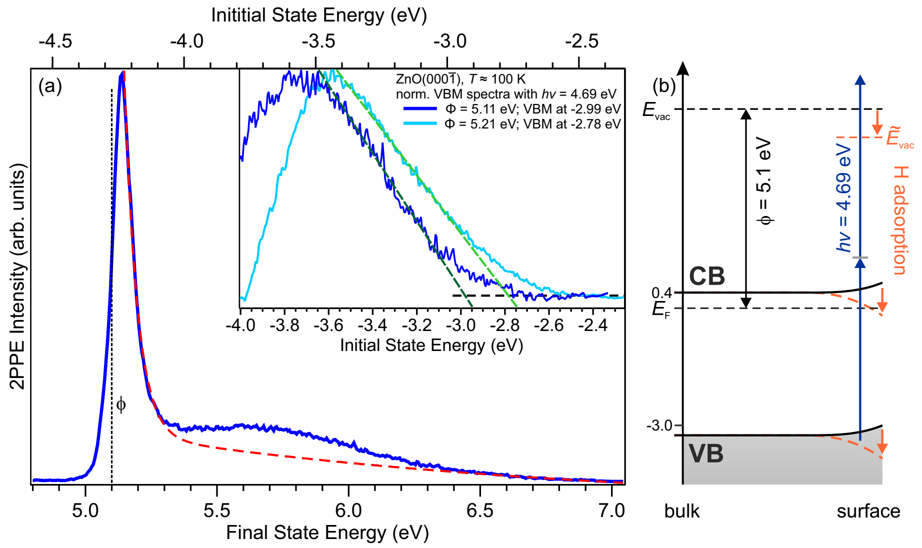

Figure 4.1.2: (a) Determination of the ZnO(000$\bar{1}$) surface valence band maximum (VBM), (b) 2PPE excitation scheme for VB spectrosopy of the clean ZnO(000$\bar{1}$) surface.

Figure 4.1.3(a) shows 2PPE spectra taken with $h\nu = 6.2$ eV of the CAL directly at E_F for increasing H dosage ranging from the pristine surface to 480 L. The signal below E_F is rising with increasing H dosage until its intensity stays nearly constant for higher dosages. Analogous to Ref. [24], this PE intensity directly below E_F can be assigned to the hydrogen-induced formation of a charge accumulation layer (CAL) at the polar ZnO(000$\bar{1}$) surface. The buildup of the CAL intensity is clearly visible in Figure 4.1.4. Here, the CAL intensity (blue curve) is plotted as a function of the dosage. As one can see, the rise of the CAL intensity is rather steep in the range of low coverages up to ca. 100 L. For increasing coverage the slope is decreasing until it comes to saturation around 500 L.

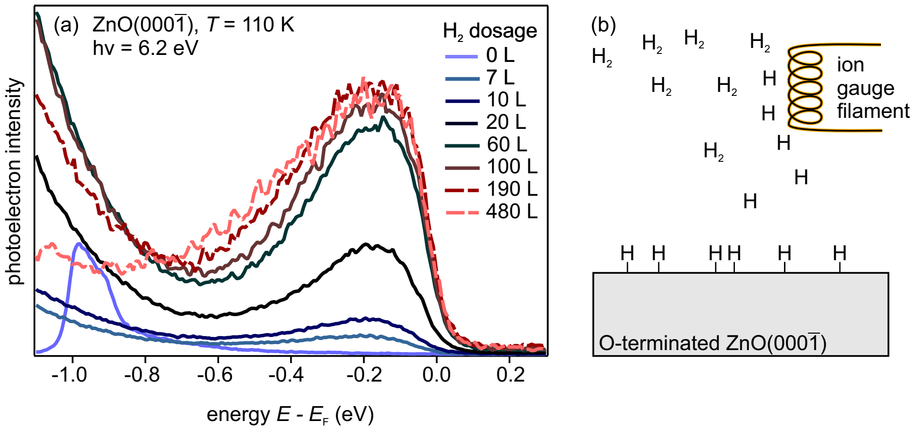

Figure 4.1.3: (a) PE signal of the CAL on ZnO(000$\bar{1}$) for increasing H dosages, (b) Scheme of the H dosing process.

Besides the rise of the CAL intensity, also the workfuntion changes due to the H adsorption. This is depicted by the black markers in Figure 4.1.4. The workfunction drastically decreases within a dosage of 100 L and subsequently reaches saturation at 3.6 eV for very high dosages of 1000 L. Notably, the observed saturations of the CAL intensity as well as the workfunction nearly coincide with each other.

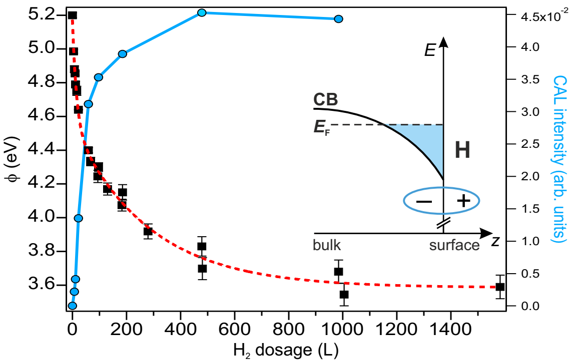

Figure 4.1.4: ZnO(000$\bar{1}$) workfunction shift and CAL formation induced by modification of the surface dipole (inset).

Hydrogen adsorption clearly changes the surface dipole and, furthermore, causes a *downward* surface band bending, which is reflected in CAL formation, which is caused by the crossing of the CBM and E_F. This behavior is most probably induced by the formation of the OH bond. The formation of the OH bond gradually lowers the surface dipole and thus the workfunction as illustrated by the inset. Within the OH bond, the electron density is primarily located at the O atom giving rise to a strongly polarized bond with its positive end reaching out into the vacuum. The saturation of the workfunction shift and CAL intensity, in this picture, corresponds to a saturation of the sample surface with hydroxyl groups. Note that this does not necessarily mean that each oxygen atom is terminated. Instead, the sample reached its thermodynamic equilibrium with the surrounding at the given background pressure.

In addition to the mentioned observations, there is another feature emerging in the spectra. This is shown in Figure 4.1.5(a), which depicts a spectrum of the 96 L H/ZnO(000$\bar{1}$) surface before (solid line) and after background substraction (dashed line). It clearly shows a peak 1.4 eV below E_F, i.e. in the band gap of ZnO. Due to its energetic position below E_F, this peak is only detectable for $\Phi < 4.6$ eV using a photon energy of $h\nu = 6.2$ eV. For higher workfunctions, this signal is cut by the secondary electron cut-off.

The appearance of in-gap states at oxide surfaces is well-known []. In the case of bulk ZnO these are primarily attributed to defect states, which are dominated by O-vacancies []. For the removal of an O species (atomic or ionic) the bonds to the neighboring atoms are broken and the vacant site is then filled with the number of electrons depending on the character of the O species. The binding energy of 1.4 eV determined for the state shown in Figure 4.1.5(a) is in reasonable agreement with V_O and V_{OH} defect states from the literature [38], and thus labeled as $V_{O/OH}$.

The electronic levels for the polar ZnO(000$\bar{1}$) surface upon H adsorption are schematically depicted in Figure 4.1.5(b). Hydrogen adsorption induces the formation of a CAL by

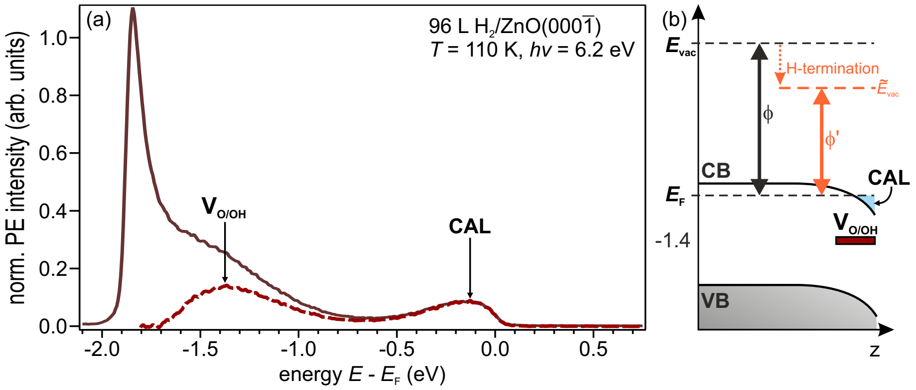

Figure 4.1.5: (a) Signature of O vacancies and CAL on the ZnO(000$\bar{1}$) surface (b) Comprehensive energy diagram of ZnO(000$\bar{1}$)

downward band bending of the CBM below E_F. This CAL formation and the simultaneous reduction of the workfunction Φ can be followed with PE spectroscopy. Additionally, the reduction of Φ allows for the observation of in-gap states, which can be attributed to O and OH vacancies $V_{O/OH}$.

4.1.1 Comparison of the polar and nonpolar ZnO surfaces

In this section, the electron energetics of the polar ZnO(000$\bar{1}$) and the nonpolar ZnO(10$\bar{1}$0) are compared for the clean surfaces as well as their behavior toward H exposure.

As described in Section 2.1, the workfunction Φ is a surface specific property. It is therefore expected to observe different values for Φ on the respective pristine surfaces. While on the nonpolar (10$\bar{1}$0) surface Φ is 4.50(5) eV, the polar (000$\bar{1}$) surface exhibits an increased value of 5.20(5) eV. This difference can be attributed to the polarity of the O-terminated (000$\bar{1}$) surface.

Despite the differences in the workfunction and the direction of the initial surface band bending (upward on (000$\bar{1}$) and downward on (10$\bar{1}$0)), the response to hydrogen exposure is rather similar. It leads to H adsorption on both surfaces and the formation of OH bonds, in which the electron density is mostly localized at the O atom. At these sites, the surface potential is significantly lowered, leading to the effect of surface downward band bending of the CBM and thus results in a CAL directly below E_F. The formation of this CAL, as well as the accompanied workfunction shift induced by H adsorption was investigated for increasing H dosage. The combined results of both ZnO surfaces are shown in Figure 4.1.6 as a function of the H exposure.

The workfuntion Φ on both surfaces, shown by the filled squares, is strongly reduced upon H adsorption up to $\Delta\Phi_{\max} = -0.65(5)$eV for ZnO(10$\bar{1}$0) and $\Delta\Phi_{\max} = -1.60(5)$eV for ZnO(10$\bar{1}$0). On the nonpolar surface, the major reduction occurs at low H dosages < 50 L followed by a saturation of the shift for dosages higher than ≈ 150 L. On the contrary, the workfunction decreases significantly slower at the polar surface and saturation is reached

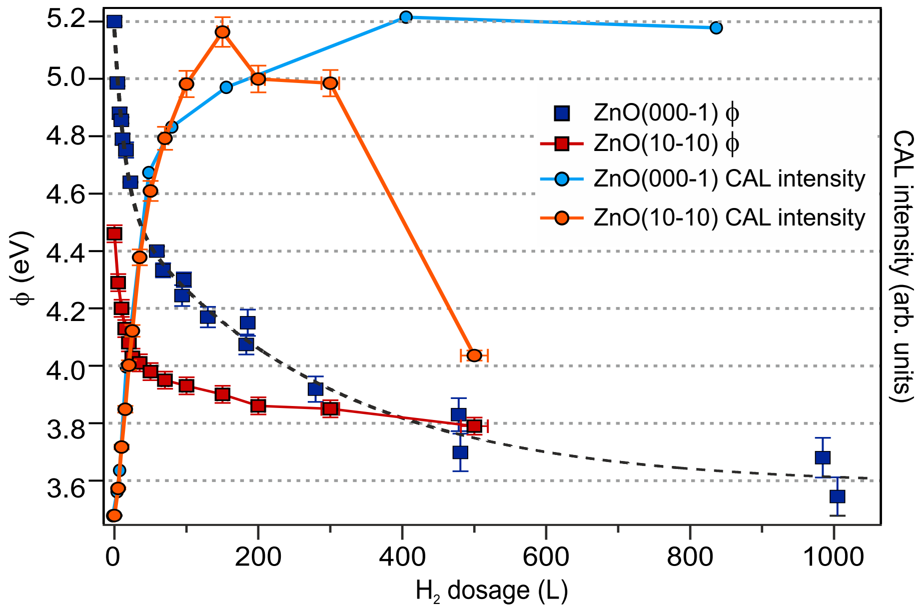

Figure 4.1.6: Workfunction and CAL intensity for ZnO(000$\bar{1}$) and ZnO(10$\bar{1}$0) as a function of H dosage.

at very high dosages of 900 L.

Along with the reduction of Φ the intensity (normalized) of the CAL is shown in filled circles. On the nonpolar surface (orange circles) the CAL intensity drastically rises for dosages up to 150 L. Further H dosing subsequently leads to a reduction of the CAL intensity. The maximum of this intensity nearly coincides with the saturation of the respective Φ(red squares). On the polar surface (blue circles) the drastic increase of the CAL intensity is very similar. The intensity, however, exhibits a *saturation* which roughly coincides with the minimum Φ(blue squares).

Besides the polarity, the most obvious difference between the surfaces is the presence/absence of Zn atoms. In the case of the mixed-terminated surface, this leads to a competition of adsorption at the O and the Zn sites. DFT calculations [25] show that for low coverages, the O atoms are the favored adsorption sites. With gradually increasing dosage the adsorption on Zn gets more likely. Ref. [25] also shows that the formation of a ZnH bond has a complementary effect compared to that observed for the OH bond. Due to the formation of the ZnH bond, electron density is transferred from the Zn atom toward the H, thereby the surface potential is enhanced, resulting in a lower $\Delta\Phi$. At a dosage > 150 L the antagonizing adsorption mechanisms reach a quasi-equilibrium state, in which the surface dipole, and thus the workfunction, do not change any further, while the CAL intensity still decreases. For further coverages, interactions between neighboring adsorption sites need to be taken into account and the simplified picture of two independent adsorption sites of counteracting character turns into a more complex adsorption mechanism. In addition, the charge distribution gets more complex, as the surface dipole remains constant but the CAL intensity reduces, which could possibly be achieved by *lateral* charge redistribution

On the O-terminated ZnO(000$\bar{1}$) surface the situation is different: The concentration of surface Zn atoms can be neglected, as well as the competition of adsorption sites, which leads only to the OH formation and the reduction of the workfunction.
As previously described in Section 4.1, on the ZnO(000$\bar{1}$) $\mathrm{V_{O/OH}}$ defect states could be observed at 1.4 eV binding energy in the PE spectra with $h\nu = 6.2$ eV and $\Phi < 4.6$ eV. Since, these defect states are assigned to O vacancies on the surface, these states should be observed on the nonpolar surface as well. In fact, in early PE spectra ($h\nu = 6.2$ eV) of the H covered ZnO(10$\bar{1}$0) surface by J.-C. Deinert, a slight increase in intensity could be reckoned around 1.4 eV binding energy. However, most of the signal in this region is overshadowed by the secondary electron background making a clear assignment difficult. With respect to surface termination of the nonpolar surface, consisting of stoichiometric amounts of Zn and O atoms, the concentration of surface O atoms, as the origin of $\mathrm{V_{O/OH}}$, is lower compared to ZnO(000$\bar{1}$). It seems like the $\mathrm{V_{O/OH}}$ concentration at the mixed-terminated surface is not high enough to observe a distinct feature in the spectra. This emphasizes the well defined structure and low defect concentration of the ZnO(10$\bar{1}$0) surface reported in Ref. [5].

4.2 Ultrafast electron relaxation and surface exciton formation dynamics

In order to test for the observation of excitonic state previously described for the nonpolar ZnO($10\bar{1}0$) surface in Section 2.4, we performed time-resolved two-photon photoemission (tr-2PPE) experiments on the ZnO($000\bar{1}$) surface. Here, electrons from the ZnO VB are excited across the band gap into the CB via a pump pulse ($h\nu_{\text{pump}} = 3.8$ eV) and subsequently probed by a second pulse ($h\nu_{\text{probe}} = 4.65$ eV) at varying time delays. A representative measurement is shown in Figure 4.2.1. It is a 2D false color plot of the photoemission intensities in dependence of the intermediate, state energy $E - E_{\text{F}}$ and the pump-probe delay. For background substraction the spectrum at -300 ps pump-probe delay was used, i.e. the depicted 2D spectrum exclusively shows the hot electrons excited into the CB by $h\nu_{\text{pump}}$. We observe a broad intensity distribution at zero time delay (t_0) which decays really fast within 0.2 ps, followed by a long-lived signal, which exceeds several 100 ps (not shown). Very similar to the dynamics observed at the ZnO($10\bar{1}0$) surface, the photoemission intensity also rises *below* E_{F}. Overall, the time-resolved 2PPE spectra of ZnO($000\bar{1}$) resemble very much the behavior of the photoexcited electrons at the ZnO($10\bar{1}0$) surface shown in Section 2.4.

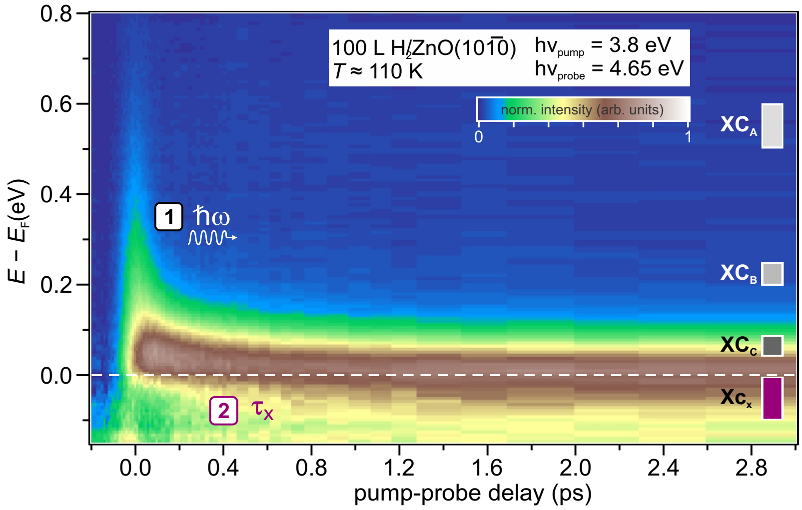

Figure 4.2.1: Dynamics of photoexcited electrons on the ZnO($000\bar{1}$) surface.

In order to gain an insight in the relaxation times of the excited electrons in the CB, cross correlation (XC) traces were taken, i.e. the PE signal was integrated over distinct energy intervals and plotted as a function of the pump-probe delay. A representative plot of the XC traces is shown in Figure 4.2.2(a). These XCs (XC_{A} to XC_{X}) correspond to the integrated signal over the energy intervals marked by boxes in the previous Figure 4.2.1. In Figure 4.2.2(a) the PE intensity is depicted as a function of the pump-probe delay for excited electrons with energies above E_{F} (circles) and for SX (diamonds) below E_{F}.

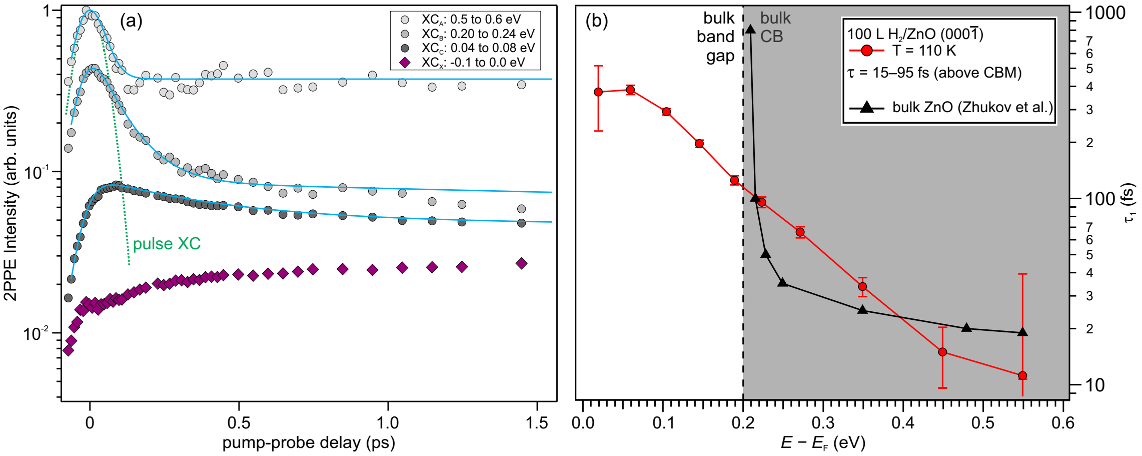

Figure 4.2.2: (a) XC traces and (b) electron relaxation times

The excited electron dynamics can be fitted using an empirical fit-function consisting of a bi-exponential decay convolved with the laser pulse's XC (green dashed)[2], which is described by squared hyperbolic secant function (sech^2).

$$I_{\mathrm{PE}}(\Delta t) = \int XC(t-\Delta t)R(t)dt \tag{4.2.1}$$

$$R(t) = \begin{cases} t \geq 0: & A_1 e^{-\frac{t}{\tau_1}} + A_2 e^{-\frac{t}{\tau_2}} \\ t < 0: & A_{\mathrm{he}} e^{-\frac{t}{\tau_{\mathrm{he}}}} \end{cases} \tag{4.2.2}$$

In the applied fit-function the fast component τ_1 characterizes the ultrafast relaxation and the second component τ_2 accounts for the contribution of the long-lived signal. The time constant τ_{he} describes the onset of the dynamics of the electrons excited by the inverse pump-probe scheme at negative time delays.

In Figure 4.2.2(b) the resulting τ_1 for the excited electrons is plotted as a function of their energy with respect to E_{F}. As the dynamics are a result of above band gap excitation, the gray-shaded area indicates the position of the bulk CB. Highly excited electrons in the region of the bulk CB ($E \geq$ 0.2eV) exhibit ultrafast τ_1 from 15 to 95 fs. For energies below 0.2 eV τ_1 increases up to several hundred fs. This qualitative similarity with the dynamics observed for the mixed-terminated surface suggests that electron relaxation occurs also in the case of the ZnO(000$\bar{1}$) surface mainly through scattering with optical phonons, as discussed in the following.

In addition to the time constants determined in our experiment, Figure 4.2.2(b) also shows the theoretical relaxation times computed by Zhukov et al. [26]. In Ref. [26], electron relaxation times were calculated for above band gap electrons in bulk ZnO. They predicted the occurrence of two types of dynamics of the excited electrons. An ultrafast relaxation

---

[2] XC of the laser pulses is obtained independently by tr-2PPE on the Ta sample holder. Highly excited electrons in virtual intermediate states possess infinitesimal lifetimes. The XC of these highly excited electrons thus gives the real convolution of the two laser pules.

time in the fs regime for electrons with energies above 70 meV through efficient scattering with a longitudinal optical phonon with this energy followed by ps dynamics close to the bulk CBM (below the phonon bottleneck energy).

The fs dynamics observed in the experiment for $E - E_\mathrm{F} > 300$ meV are in very good agreement with the calculations of Zhukov et al.. For lower energies, the observed dynamics, which are still in the fs regime, drastically differ from the theoretical predictions. This difference most probably originates from the fact that the literature refers to the bulk material: In Ref. [26], the slow ps dynamics are attributed to the strongly reduced phase space close to the CBM, where scattering with the 70 meV phonon is suppressed. On the ZnO(000$\bar{1}$) *surface* this phase space reduction does not occur due to the H induced downward bending of the CB. The excited electrons can continuously scatter to lower energies until they reach the Fermi energy.

The dynamics below E_F (diamond-shaped markers in Figure 4.2.2(a) integrated over -0.1 eV to E_F) are significantly different compared to the ones above. At zero time delay t_0, the PE intensity below E_F is relatively low [3]. With increasing time delay, it increases within several hundred fs, thus reflecting an increasing density of states (DOS) below E_F. This emergence of additional, photoinduced DOS in the already occupied electronic structure qualitatively resembles the observations on the (10$\bar{1}$0) surface (see Section 2.4), where it was attributed to the formation dynamics of a surface exciton (SX).

In order to confirm this assessment, a test experiment was performed, similar to the one discussed in Section 2.4. Apart from exciton formation, a photoinduced intensity increase below E_F could result from surface photovoltage, where photoexcitation changes the surface band bending. These two mechanisms can be distinguished by changing the excitation density: If surface photovoltage were the origin of the photoinduced intensity increase , this effect should become stronger when the excitation density is *increased*, while the relative intensity below E_F should be *reduced* if exciton formation were the origin: At densities near the Mott limit, the screening of the Coulomb interaction between the excited electrons and holes sets in and they can no longer be described in terms of non-interacting quasiparticles [12]. The literature values for the Mott limit at ZnO vary from $1.5 - 6 \times 10^{18}\mathrm{cm}^{-3}$ [2, 3, 4]. The excitation density depends on the laser fluence (photons per cm^2) and thus can be simply varied by changing the incident laser power via filters (spot size is not affected). The results of this experiment are shown in Figure 4.2.3. The blue (red) curves indicate the signal at lower (higher) excitation densities. The data clearly shows that the relative intensity below E_F is *reduced* when increasing the excitation density.

This behavior clearly shows the excitonic nature of this signal. For excitation densities near the Mott limit, the total concentration of electron-hole pairs is significantly high to enable interactions between them and result in an electron-hole plasma (EHP). In this

---

[3] The small spike in the intensity at t_0 is an artifact of the same dynamics, which are cut-off by the secondary edge, induced by the inversion of $h\nu_\mathrm{pump}$ and $h\nu_\mathrm{probe}$ for negative delays.

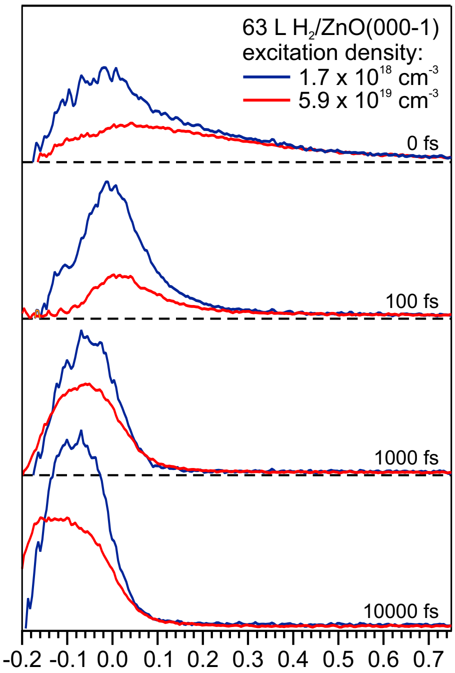

Figure 4.2.3: Signal of excited electrons excited below and near the Mott limit

collective state, the Coulomb interaction between electron and hole is screened, resulting in a reduced exciton binding energy and a reduced formation probability, respectively. For even excitation densities exceeding the Mott limit, the e-h pair formation probability should vanish and the excitonic signal should not be detected anymore.

It is, thus, concluded that the signal observed on the H covered polar ZnO$(000\bar{1})$ surface can be, analogously to Ref. [24] and discussed in Section 2.4 for the nonpolar ZnO$(10\bar{1}0)$ surface, identified to be the SX species.

The observations of the energy level alignment and ultrafast dynamics at the polar ZnO$(000\bar{1})$ surface are schematically depicted in Figure 4.2.4. In the 2PPE experiment, electrons are excited by $h\nu_{\mathrm{pump}}$ into non-equilibrium states in the CB. There, two types of dynamics are probed: (1) the ultrafast electron relaxation toward E_{F} via scattering with optical phonons within several hundred fs and (2) the formation of surface excitons (SX) below E_{F}, which exhibit lifetimes exceeding several 100 ps. The position of SX below E_{F} is hosted by the downward surface band bending induced by H adsorption.

4.2.1 Charge density-dependent electron relaxation dynamics

While the static electronic structures of the investigated surfaces show some differences, such as the opposite band bending, the workfunction and their behavior upon hydrogen adsorption, i.e. the saturation of the CAL on ZnO$(000\bar{1})$ contrasting the CAL decrease on ZnO$(000\bar{1})$ for higher coverages, the dynamics via above band gap excitation on the

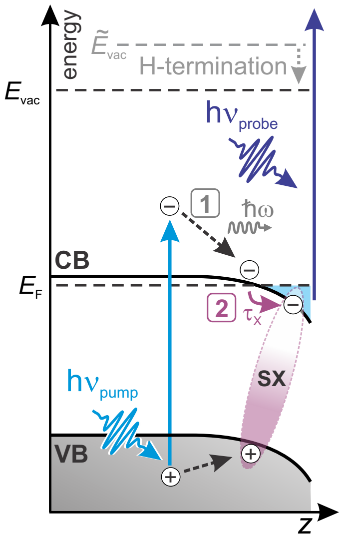

Figure 4.2.4: Energy diagram showing the photoinduced dynamics on the H/ZnO(000$\bar{1}$) surface detectable in the tr-2PPE experiment.

nonpolar (10$\bar{1}$0) and polar (000$\bar{1}$) surface are qualitatively similar (see Figures 2.4.7 and 4.2.1).

Since the observed dynamics are correlated to the existence of the CAL on both surfaces, the pretreatment described at the end of Section 4.1 is applied in all tr-2PPE experiments. It should be pointed out, that to tune the workfunctions required for the experiment, different amounts of hydrogen were needed, respectively. A comparison of the ultrafast dynamics on both surfaces, which includes the effect of the H dosage, is given in Figure 4.2.5. The figure presents the fast time constant τ_1 as a function of the energy with respect to E_F for ZnO(10$\bar{1}$0) with H coverages of 6 L (blue) and 40 L (green) and for ZnO(000$\bar{1}$) with a H dosage of 100 L (red). Qualitatively, all curves show fast time constants in the range of a few fs for high energies in the gray shaded area, which marks the position of the

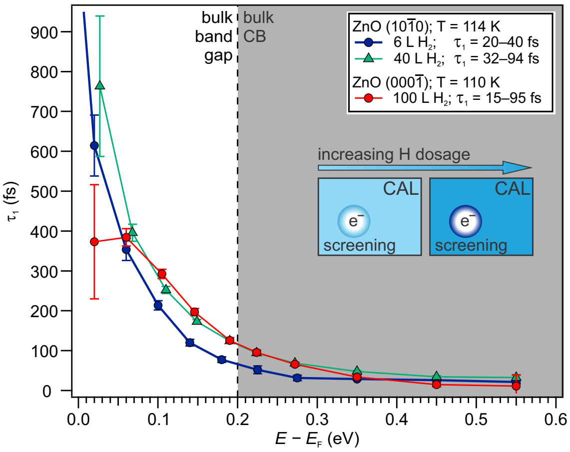

Figure 4.2.5: Fast time constant τ_1 on the polar and nonpolar ZnO surface for different H dosages/CAL densities.

bulk CB, and for lower energies τ_1 increases up to several hundred fs. Especially for high energies > 0.3 eV τ_1 is nearly identical for all curves. For energies < 0.3 eV the curves separate. On the nonpolar surface with 6 L H (blue) τ_1 is faster and exhibits values from 20 - 40 fs in the bulk CB . Whereas the behavior of the higher covered $(10\bar{1}0)$ surfaces (green) is lower and nearly congruent with the curve of the highly covered $(000\bar{1})$ surface (red), exhibiting time constants form 15 to 95 fs within the energie range of the bulk CB. Regarding the relaxation times on the ZnO$(10\bar{1}0)$ surface covered with 6 L and 40 L of hydrogen, they significantly differ for energies lower than 0.3 eV. Apperently the relaxation times on the higher covered surface are higher, i.e. the relaxation is slowed down.

Since the relaxation is related to a coupling of the excited electrons to phonons, an increased relaxation time would result from a weakening of the electron-phonon coupling. With respect to the results on the CAL, presented in Section 4.1.1, the CAL density should be increased for the 40 L coverage. So, the observation of a slowed electron relaxation is most probably connected to the difference of the CAL density. In the case of a higher charge density in the CAL, a screening of the excited electrons probably damps the coupling to phonons. The inset in Figure 4.2.5 schematically depicts the suggested screening effect with increasing H dosage, i.e. increasing CAL density respectively.

When comparing the situation of the H/ZnO$(10\bar{1}0)$ and H/ZnO$(000\bar{1})$ surfaces with coveraes of 40 L and 100 L respectively, they show comparable workfunctions. This in turn, points toward a comparable modification of the surface dipole by the CAL. In addition, the relaxation times are remarkably similar for both surfaces. Hence, these observation suggest the formation of comparable electronic structures on both surfaces for the respective hydrogen termination with a almost equally pronounced screening effect. Furthermore, the resemblance of the relaxation times of excited electrons for the different surfaces seems to be determined by the electronic effects rather than their respective structures.

In conclusion, the influence of hydrogen adsorption on the polar O-terminated ZnO$(000\bar{1})$ was investigated with time-resolved photoelectron spectroscopy. The H adsorption leads to the formation of hydroxyl (OH) bonds at the surface and a strong modification of the surface dipole by charge redistribution, accompanied by a pronounced decrease of the worktion of $\Delta\Phi = 1.6$ eV. In addition, the surface electronic structure changes from an initial upward band bending to an upward band bending below E_{F}, which leads to a surface metallic state, the charge accumulation layer (CAL). Accept for the CAL, the photoelectron spectra also show a signal of surface oxygen vacancies $\mathrm{V}_{\mathrm{O/OH}}$ at a binding energy of 1.4 eV with respect to $E_{[\mathrm{F}}$.

Comparison to a previous study on the mixed-terminated ZnO$(10\bar{1}0)$ surface [24], in which the CAL formation is also observed, shows that the magnitude of $\Delta\Phi$ and the behavior of the CAL for higher hydrogen dosages depends on the presence of Zn atoms on the surface. While the CAL intensity is reduced for the Zn containing ZnO$(10\bar{1}0)$ surface, the CAL saturates at the ZnO$(000\bar{1})$ surface.

Using time-resolved 2PPE spectroscopy, two types of dynamics induced by above band gap excitation can be seen, ultrafast electron relaxation by electron-phonon scattering in the conduction band and the slower photoinduced formation of density of states below E_F. Analogous to the observations on ZnO$(10\bar{1}0)$, it could be shown that the additional DOS below E_F can be ascribed to the formation of a long-living surface exciton SX, whose stability arises from its energetic position with respect to E_F, which is a direct result of the adsorption-induced surface band bending. Furthermore, it could be shown that the electron relaxation dynamics in the CB are sensitive to the density of the CAL. Independent of both surfaces, the electron-phonon coupling is modified by the CAL density, which can be controlled by the H dosage. A higher CAL density leads to screening of the electron-phonon coupling, which enhances the excited electron lifetimes.

5 Strong intermolecular coupling of excitons in organic dyes on ZnO surfaces

In this section first experiments on the electron dynamics at the interfaces of SP6 with ZnO($10\bar{1}0$) and ZnO($000\bar{1}$) are presented. Since this is an ongoing project, the presented results shall give an overview on our observations of the organic/inorganic hybrid sytem: For our measurements, we first prepared the respective ZnO surface as described in Section 4.1, followed by deposition of SP6 with the Knudsen-type effusion cell onto the surface. SP6 was sublimated at a base temperature of 570 K while the sample was kept at 300 K. A quartz microbalance (QMB) was used for the controlled preparation of films. The determination of the film thickness was done with the Sauerbrey equation, which describes the frequency change Δf of an piezoelectric oscillating quartz crystal as a function of its mass change Δm upon deposition [39].

$$\Delta f = -\frac{2f_0^2}{A\sqrt{\rho_\mathrm{q}\mu_\mathrm{q}}}\Delta m. \tag{5.0.1}$$

Here, f_0 is the start frequency, A the area of the quartz crystal, ρ_q the density of quartz, and μ_q is the shear modulus of quartz ($z_q = \sqrt{\rho_\mathrm{q}\mu_\mathrm{q}}$). Under the assumptions that the deposited mass is rigid, evenly distributed and $\Delta f \ll f$ the coverage θ can be determined by

$$\theta = \Delta f \cdot \frac{z_q}{\rho_{molecule} 2 f_0^2} \cdot \gamma, \tag{5.0.2}$$

with $\rho_{molecule}$ being the density of the molecule and γ as the tooling factor, which describes the ratio of Δf for direct deposition onto the QMB and indirect deposition with the sample placed in front of the QMB.

The study started with rather thick films of 20 nm of SP6 on ZnO($10\bar{1}0$), similar to the samples of Foglia et al. (see Section 2.5) in order to first characterize the dynamics in bulk SP6 and its vacuum interface. In order to ascribe the observed SP6 PE signal to the occupied or unoccupied electronic structure, we performed measurements with various photon energies. The results of this photon energy dependence are shown in Figure 6(a). Here, the PE intensity is displayed as a function of the kinetic energy for the SP6 signal

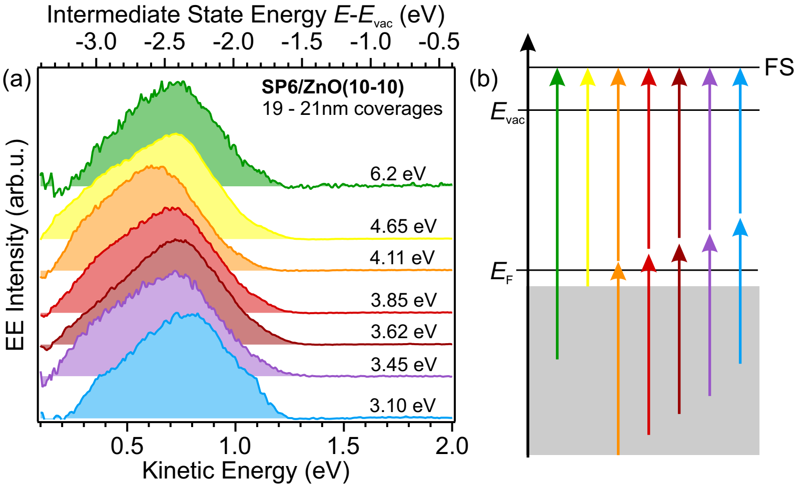

Figure 6: Photon energy dependence of 20 nm SP6 on ZnO($10\bar{1}0$).

after subtraction of the secondary electron background as described in Section 4.1. The photon energy was varied from 3.1 to 6.2 eV. Notably, the workfunction of 20 nm SP6 was determined to be 3.4 eV, which would result in direct photoemission for most excitation energies. Regarding the relatively wide interval of photon energies, major shifts of the signal were expected in either case. However, the PE signal in Figure 6(a) does not shift and exhibits the essentially the same energy distribution. A possible mechanism to explain this independence of the photon energy is the the population of final states above the vacuum level via photoemission. It should be noted, that this would require a very broad continuum of initial states below E_F (gray shaded area) as illustrated in Figure 6(b). Such scenario does not appear probable for a molecular film.

Assuming a “2PPE-like” process, two kinds of PE experiments were performed, to check this possible excitation pathway: An excitation fluences dependence and a pulse length dependence. In a 2PPE process with a photon energy $h\nu = 3.6$ eV[1] (purple arrow in Figure 6(b)), the population of a final state and thus its amplitude should exhibit a square dependence of the excitation fluence. However, the analysis of the amplitudes for increasing excitation fluence yielded a power law with an exponent of 1.5. This suggests, that the observed electron emission signal might not be produced in a pure 2PPE process, and thus, might not result from a final state.

In the pulse length dependence, the 3.6 eV pulse length was varied from 54 to 189 fs. For a 2PPE process, the PE intensity should exhibit a significant decrease with increasing pulse length , as two photons within one pulse would be required to probe the dynamics. Instead, no variation of the signal intensity was observed. This independence of the pulse length proves the absence of a final state probed by 2PPE. Furthermore, it suggests the observation of a long-lived state with a lifetime exceeding the temporal separation of two

---

[1] In case of direct photoemision, the spectra should exhibit a broadening of 0.2 eV. Since, the observed spectra in Figure 6 exhibit a larger broadening, the process must be involve the absorption of two energy quanta.

subsequent laser pulses given by the repetition rate of the laser.

In order to shed light into the origin of this spectral feature, the repetition rate of the laser was varied. As illustrated in Figure 7, a signal resulting from a long-lived state that remains populated for times exceeding the inverse of the repetition rate should drop when reducing the repetition rate, i.e. increasing the time delay between two consecutive pulses.

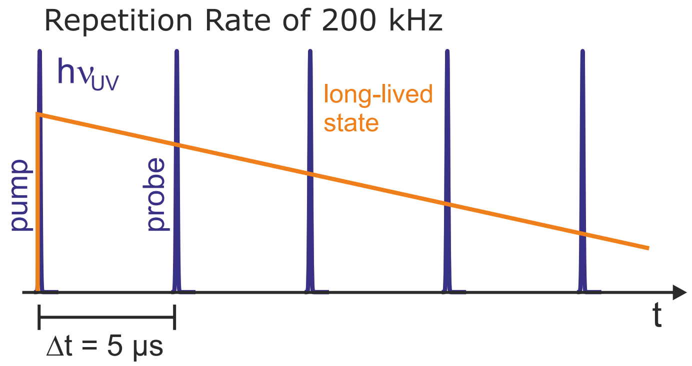

Figure 7: Excitation and probe scheme of a long-living state exceeding the repetition rate of the laser (200 kHz).

The result of this measurement is shown in Figure 8. The figure 8(a) displays the normalized emission signal of a 28 nm thick film of SP6 as a function of the kinetic energy for two different repetition rates, 200 (red) and 40 kHz (blue). As one can clearly see, with decreasing repetition rate the overall signal intensity is reduced. Considering the time delay between adjacent pulses for the different repetition rates, which is 5 and 25 µs respectively, the long-lived state exhibits lifetimes longer than 25 µs. Relating this result with what is known about the ultrafast dynamics in SP6 described in Section 2.5, we attribute this state to the dark state (DS) of SP6, which was also observed to survive the inverse of the laser repetition rate in previous optical experiments [33].

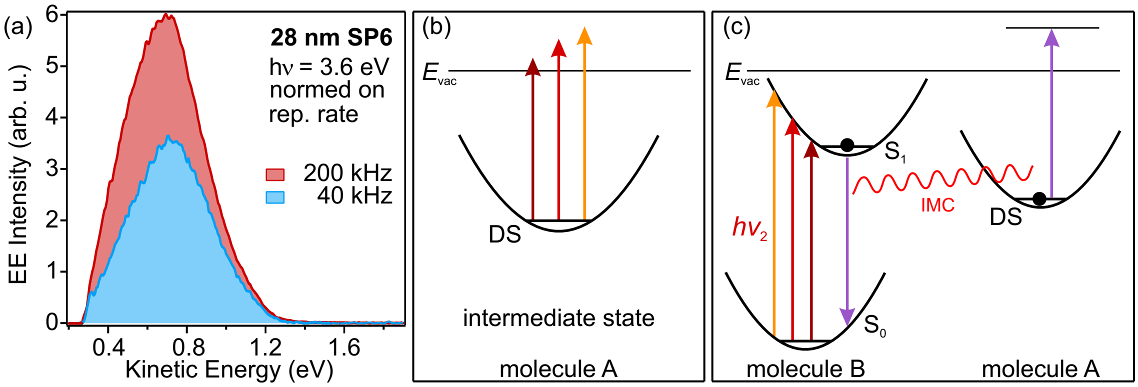

Figure 8: (a) PE signal of 28 nm SP6 on ZnO(10$\bar{1}$0) for 200 (red) and 40 kHZ (blue) (b) Photoemission from an intermediate state (c) Electron emission via intermolecular coupling.

As mentioned above, the photoemission from the DS is independent of the photon energy $h\nu_{\text{probe}}$. This does not agree with photoemission from a long-lived intermediate state (cf.

Figure 8(b)). Instead, the emission of electrons of a fixed kinetic energy must be triggered by a distinct amount of energy other than $h\nu_{\text{probe}}$ that is an intrinsic characteristic of the system. In such a scenario, different excitation energies would not alter the energetic position of the spectral signature as illustrated in Figure 8(c). The dark state is populated in one molecule and probed by intermolecular coupling after excitation by the next laser pulse $h\nu_2$.

Based on the results from optical spectroscopy of this system on the electronic structure and dynamics introduced in Section 2.5, there are two types of excited states potentially relevant for intermolecular coupling, the S_1 and the DS itself. The possible coupling scenarios are schematically depicted in Figure 9. Figure 9(a) shows the energy levels of two photoexcited molecules A and B. Photoexcitation with $h\nu_1 = 3.6$ eV creates a population of the DS in molecule A. When the next pulse $h\nu_2$ arrives at the sample after 5 µs, the DS of molecule B is populated. Electron emission from DS at molecule A is achieved by energy transfer via intermolecular coupling (IMC) to DS, accompanied by electron relaxation to the ground state in molecule B. Figure 9(b) shows the analogous scheme for coupling between the DS of molecule A and the S_1 of B. The DS molecule A is populated as before, whereas in B, the second pulse after 5 µs populates the S_1 state. The electronic transition of SP6 at 3.14 eV associated with $S_1 \rightarrow S_0$ participates in this scenario in the electron emission (EE). The two mechanisms can be disentangled by measuring the dynamics of the signal formation: If it were related to the DS-DS transition, a simple µs decay would be expected as both DS population dynamics in molecule A and B occur on µs timescales. On the other hand the S_1-DS coupling would lead to a double exponential decay with a 200 ps and a µs time constant, because the ps dynamics of the S_1 state would be convolved with the µs dynamics of the DS.

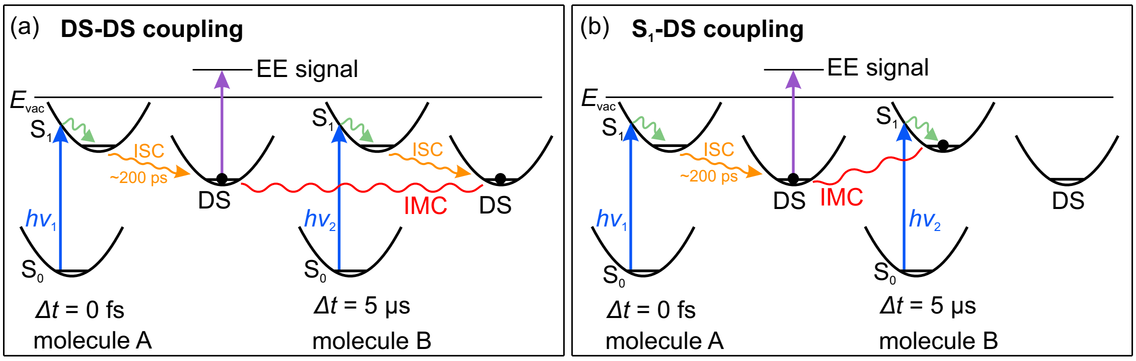

Figure 9: (a) Intermolecular DS-DS coupling (b) Intermolecular S_1-DS coupling.

In order to gain insight into the time scales involved in the formation of the dark state, we performed an autocorrelation tr-2PPE experiment with $h\nu_{\text{pump/probe}} = 3.85$ eV. A scheme of this experiment is displayed in Figure 10. Similar to the repetition rate experiment, the population of the long-lived DS (yellow) is induced by $h\nu_{\text{pump}}$. But, complementary to the previous experiment, which enabled visualization of the DS signal on µs timescale, the

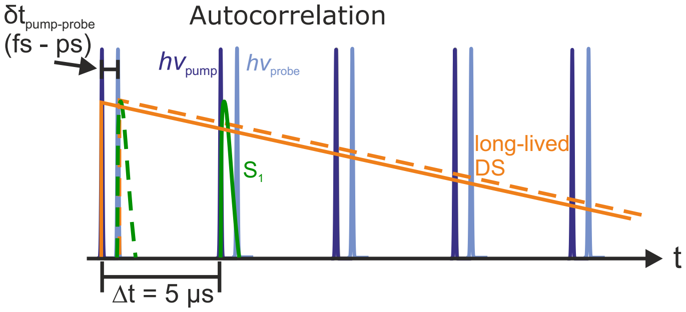

Figure 10: Schematic description of the autocorrelation experiment of SP6 with $h\nu = 3.85$eV.

autocorrelation approach gives access to the dynamics in fs and ps timescale implementation of $h\nu_{\text{probe}}$[2]. Additionally the ps population of S_1 (green)[3], which can also be induced with $h\nu_{\text{pump}}$ is depicted. With respect to the possible coupling mechanisms, the expected system response for the DS-DS would be a convolution of the DS population (yellow) with itself by photoexcitation with $h\nu_{\text{probe}}$, yielding µs dynamics. Whereas, the expected response for the S_1-DS coupling would be given as a convolution of the DS population with the ps S_1 population. This would lead to the observation of ps and µs dynamic in the autocorrelation spectrum. The results of this measurement are qualitatively depicted in Figure 11.

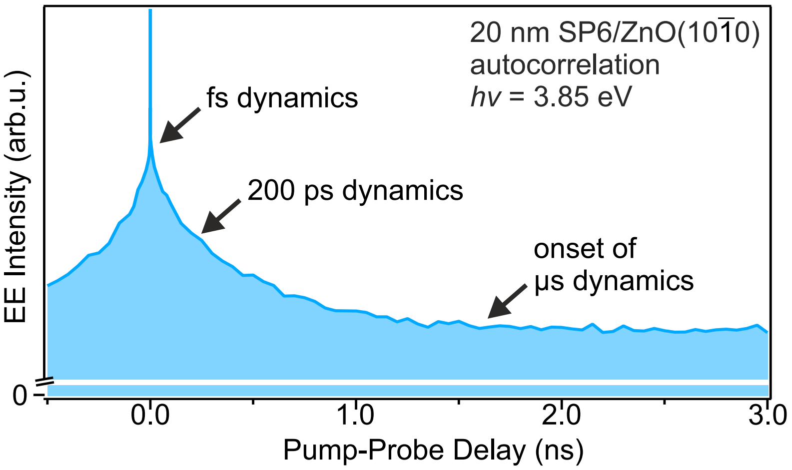

Figure 11: Integrated signal of the autocorrelation experiment of SP6 with $h\nu = 3.85$eV.

The electron emission intensity is displayed as a function of the pump-probe delay (ns). It should be noted, that for better illustration the intensity axis is rescaled. The amplitudes of the dynamics are small (~ 10 %) compared to the background offset, which results from the stationary background of the two beams. Around zero time delay a high intensity signal which decreases on a fs time scale can be seen, followed by dynamics on 200 ps timescale. For time delays longer than 1 ns, the intensity exhibits a constant offset.

Note that it is, *per se*, not possible to disentangle between electron emission through (i)

---

[2] Since $h\nu_{\text{pump}} = h\nu_{\text{probe}}$, photoexcitation induces the same dynamics for varying time delay.

[3] For illustrative purposes, the population of S_1 is not displayed to scale.

absorption of a laser photon or (ii) intermolecular coupling (IMC). Both can contribute to the electron emission spectra. With regard to the spectral signature around 0.8 eV kinetic energy, it is, however, known from the photon energy dependence experiment in Figure 6 that it must originate from electron emission from the DS, which is populated on a 200 ps timescale and survives for µs. This allows for the following two assignments: (i) The fs dynamics to electron relaxation cannot be related to the much slower built-up population of the DS and are, thus, probed in a pure 2PPE process. They are probably connected to the fast vibrational relaxation in the S_1 state. (ii) The ps dynamics observed in the autocorrelation experiment on the other hand should mainly be influenced by IMC to the singlet S_1 population. If it were probed by laser photons, it should expose a spectral shift upon energy variation, which it does not. Time-resolved optical measurements by Foglia et al., showed that the ps dynamics are related to the population decay of the S_1 via competing pathways: luminescence, formation of DS via intersystem crossing (ISC) and diffusion toward the ZnO interface. These dynamics are followed by a plateau for longer time delays, related to the onset of the µs dynamics of DS.

Since in this experiment, the ps dynamics are clearly visible, the emission of the electrons in DS can be assigned to the intermolecular coupling to the S_1 population as shown in Figure 9(b) and not to IMC to the DS excited by $h\nu_2$. Possible scenarios for this energy transfer would be related to either a radiative process, i.e. luminescence, or non-radiative processes, such as Förster resonance energy transfer (FRET) or intermolecular Coulombic decay. Assignment of either process is based on the current results, not possible. Since all these mechanisms exhibit a distinct distance dependence, possible test experiments would involve a modulation of the distance between excited molecules. For instance, to distinguish between radiative coupling, which can occur over wide distances, and non-radiative coupling, which is strongly distance dependent (FRET $\sim R^6$), might be the implementation of a buffer layer into the SP6 film. In a layered structure consisting of a thin film of SP6 at the vacuum interface (A) and a thick SP6 film (B), separated by a transparent buffer layer of a few nm, a non-radiative interaction between excited molecules in A and B would be blocked by the buffer layer, whereas radiatve inteaction would still enable electron emission. Another approach would be to manipulate the density of the SP6 layer by intercalating inert molecules or atoms, e.g. noble gases.

As shown above, the EE signal is related to intermolecular coupling of the S_1 population with the DS. As the $S_1 \rightarrow S_0$ transition is related to an energy loss of 3.14 eV [33], it can be assumed that EE occurs through the absorption of an energy quantum of 3.14 eV. The energy axis of Figure 6 can, thus, be rescaled in order to asses the intermediate state energy of the DS with respect to the vacuum level E_{vac}. As shown in Figure 6 (top axis), it lies at 2.5 eV. The determination of this DS binding energy goes beyond what is achievable by optical spectroscopy, which only probes relative energies.

Although the bulk SP6 exhibits relatively slow dynamics and a rather unusual electron emission process, up to this point, the results are qualitatively in agreement with the optical measurement. For a quantitative description of the involved time constants for the intermolecular coupling further analysis is required[4]. Future experiments, with a clearer picture of the dynamics in bulk SP6, target the interface formation and the photoinduced electron dynamics of SP6 with ZnO(000$\bar{1}$), and ZnO(10$\bar{1}$0) respectively.

---

[4] The construction of a suitable model for the SP6 dynamics is an ongoing project.

6 Conclusion

This work presents a characterization of the pristine and hydrogen-covered polar ZnO(000$\bar{1}$) surface and an investigation of the photoinduced electron dynamics using time-resolved two-photon photoemission (2PPE) spectroscopy. A comparison to previous investigations of the nonpolar ZnO(10$\bar{1}$0) showed similarities in their behavior upon hydrogen adsorption and upon above band gap photoexcitation. Also the photoinduced dynamics of the spirobifluorene derivative SP6 deposited on the ZnO(10$\bar{1}$0) surface were investigated.

The pristine ZnO(000$\bar{1}$) surface exhibits a workfunction of 5.15(5) eV and exhibits an upward band bending. H adsorption leads to the modification of the surface dipole by formation of strongly polarized hydroxyl (OH) bonds with their positive side reaching into the vacuum. The adsorption further induces an inversion of the surface band bending, resulting in the conduction band minimum bent below E_F, which renders density of states (DOS), which is populated due to the electron donating influence of the OH bond. In the photoemission spectrum this process can be observed by the buildup of a metallic state, the charge accumulation layer (CAL), directly below E_F as a function of the hydrogen dosage onto the surface. When following this buildup, accompanied with the workfunction downshift induced by the lowering of the surface dipole, a saturation of the CAL is observed for increasing H dosages, which is different compared to the CAL behavior on the nonpolar ZnO(10$\bar{1}$0) surface, on which the workfunction shift is less pronounced and the CAL intensity decreases for higher hydrogen dosages due to the competitive formation of electron accepting ZnH bonds.

In time-resolved 2PPE, above band gap excitation enables the observation of two types of non-equilibrium dynamics on the H/ZnO(000$\bar{1}$) surface, which resemble the dynamics recently published on the H/ZnO(10$\bar{1}$0) surface [24]: On the one hand, the ultrafast fs relaxation of excited electrons via scattering with optical phonons followed by the occurrence of additional, photoexcited states below E_F, which can be ascribed to the formation of a surface exciton species (SX). Comparison of the fs dynamics on both ZnO surfaces showed an influence of the CAL density, which is directly connected to the H dosage and the concurrent increase of charge density. With increasing CAL density, the fs dynamics are slowed down, due to a weakening of the electron-phonon coupling by enhanced screening by the CAL electrons. The resemblance of relaxation times for both H covered surfaces, ZnO(000$\bar{1}$) and ZnO(10$\bar{1}$0), as well as the SX formation strongly suggest very similar electronic structures of the two surfaces. This means that the observed ultrafast dynamics are not influenced by the structures of the respective surfaces but rather by electronic effects. On the basis of photoinduced dynamics observed in optical measurements on SP6 [33], 20 nm thick SP6 films on the ZnO($10\bar{1}0$) surface were investigated in time-resolved PE experiments. The detection of an unusual signal at 0.8 eV kinetic energy *independent* of the excitation energy first suggested the occurrence of a final state. This could be excluded by a number of test experiments. Instead, the emission signal could be assigned to originate from a long-living dark state (DS) exceeding lifetimes of 25 µs. The DS is formed on a 200 ps timescale after the population of the first singlet excited state S_1 via intersystem crossing. It is not probed by photoemission, but emission from the DS requires an intermolecular coupling to other excited states. In an autocorrelation experiment, this intermolecular coupling, occuring within hundreds of ps, could be traced back to the S_1 population. The nature of this coupling (i.e. dipole-dipole coupling or Coulombic) could not be elucidated yet and will be the subject of future investigations.

Up to now, this study yielded an understanding of the electron dynamics in SP6 on a qualitative level. However, for a quantification of the time constants of the involved processes, further analysis based on a suitable kinetic model is necessary. Furthermore, with respect to electronic coupling and interface dynamics, which are crucial aspects for possible optoelectronic applications, photoemission experiments on thin SP6 films (1 nm) on ZnO($000\bar{1}$) and ZnO($10\bar{1}0$) need to be performed.

The presented results on the electronic structure of the pristine as well as the hydrogen-covered ZnO($000\bar{1}$) surface are crucial for the understanding of energy level alignment and electronic coupling of inorganic/organic interfaces. Besides the ubiquitous hydrogen, organic molecules are based on various hydrocarbon units, the formation of a conducting charge accumulation layer at the interface of ZnO and chemisorbed molecules seems highly likely and is thus important for the application of ZnO as transparent conducting electrode material in optoelectronic devices. Moreover, the surface exciton (SX), which is hosted by the charge accumulation layer and observed on the ZnO($000\bar{1}$) as well as the ZnO($000\bar{1}$) surface, could be used for efficient Förster resonance energy transfer at the interface, which is strongly distance-dependent and, thus relies on the dipole-coupling of surface species. Especially with respect to systems based on ZnO nanoparticles, which exhibit high surface-to-volume ratios, the knowledge of the electronic structure and dynamics of the low-index surfaces dominating these particles is highly relevant. The preliminary study of the photoinduced dynamics in the organic dye SP6 shed light into the absolute energy levels in the bulk material, which is highly relevant to for interfacial energy level alignment. Furthermore, the strong light-matter coupling as well as the strong intermolecular coupling of its excited states S_1 and the long-living dark state might be relevant for light harvesting applications, as this coupling could allow the charge separation of the DS.

List of Publications

J.-C. Deinert, D. Wegkamp, M. Meyer, C. Richter, M. Wolf and J. Stähler, *Ultrafast Exciton Formation at the ZnO*$(10\bar{1}0)$ *Surface*, Physical Review Letters **113**, (2014), 057602

D. Wegkamp, M. Meyer, C. Richter, M. Wolf and J. Stähler, *Photoinduced workfunction modifications and their effect on photoelectron spectroscopy* Applied Physics Letters **103**, (2013), 151603

A. Kothe, J. Metje, M. Wilke, A. Moguilevski, N. Engel, R. Al-Obaidi , C. Richter, R. Golnak, I. Y. Kiyan and F. Aziz, *Time-of-flight electron spectrometer for a broad range of kinetic energies* Review of Scientific Instruments **84** (2013), 023106

Bibliography

[1] W. Y. Liang, "Excitons," *Physics Education*, vol. 5, pp. 226–228, July 1970.

[2] E. Hendry, M. Koeberg, and M. Bonn, "Exciton and electron-hole plasma formation dynamics in ZnO," *Physical Review B*, vol. 76, p. 045214, July 2007.

[3] A. Schleife, C. Rödl, F. Fuchs, K. Hannewald, and F. Bechstedt, "Optical Absorption in Degenerately Doped Semiconductors: Mott Transition or Mahan Excitons?," *Phys. Rev. Lett.*, vol. 107, p. 236405, Nov. 2011.

[4] M. a. M. Versteegh, T. Kuis, H. T. C. Stoof, and J. I. Dijkhuis, "Ultrafast screening and carrier dynamics in ZnO: Theory and experiment," *Phys. Rev. B*, vol. 84, p. 035207, July 2011.

[5] C. Wöll, "The chemistry and physics of zinc oxide surfaces," *Progress in Surface Science*, vol. 82, no. 2-3, pp. 55–120, 2007.

[6] P. J. Nieuwenhuizen, "Zinc accelerator complexes.," *Applied Catalysis A: General*, vol. 207, no. 1-2, pp. 55–68, 2001.

[7] P. D. C. King and T. D. Veal, "Conductivity in transparent oxide semiconductors.," *Journal of physics. Condensed matter : an Institute of Physics journal*, vol. 23, p. 334214, Aug. 2011.

[8] A. a Mosquera, D. Horwat, A. Rashkovskiy, A. Kovalev, P. Miska, D. Wainstein, J. M. Albella, and J. L. Endrino, "Exciton and core-level electron confinement effects in transparent ZnO thin films.," *Scientific reports*, vol. 3, p. 1714, Apr. 2013.

[9] S. Blumstengel, S. Sadofev, C. Xu, J. Puls, and F. Henneberger, "Converting Wannier into Frenkel Excitons in an Inorganic/Organic Hybrid Semiconductor Nanostructure," *Physical Review Letters*, vol. 97, p. 237401, Dec. 2006.

[10] . Özgür, Y. I. Alivov, C. Liu, A. Teke, M. a. Reshchikov, S. Doğan, V. Avrutin, S.-J. Cho, and H. Morkoç, "A comprehensive review of ZnO materials and devices," *Journal of Applied Physics*, vol. 98, no. 4, p. 041301, 2005.

[11] J. Fan, K. Sreekanth, Z. Xie, S. Chang, and K. Rao, “p-Type ZnO materials: Theory, growth, properties and devices,” *Progress in Materials Science*, vol. 58, pp. 874–985, July 2013.

[12] C. Klingshirn, J. Fallert, H. Zhou, J. Sartor, C. Thiele, F. Maier-Flaig, D. Schneider, and H. Kalt, “65 years of ZnO research - old and very recent results,” *physica status solidi (b)*, vol. 247, pp. 1424–1447, Apr. 2010.

[13] C. R. A. Catlow, S. A. French, A. A. Sokol, A. A. Al-Sunaidi, and S. M. Woodley, “Zinc oxide: A case study in contemporary computational solid state chemistry.,” *Journal of computational chemistry*, vol. 29, pp. 2234–49, Oct. 2008.

[14] U. Diebold, L. V. Koplitz, and O. Dulub, “Atomic-scale properties of low-index ZnO surfaces,” *Applied Surface Science*, vol. 237, pp. 336–342, Oct. 2004.

[15] O. Dulub, L. A. Boatner, and U. Diebold, “STM study of the geometric and electronic structure of ZnO(0001)-Zn, (000 -1)-O, (10 -1 0), and (11 -2 0) surfaces,” *Surface Science*, vol. 519, pp. 201–217, Nov. 2002.

[16] O. Dulub, U. Diebold, and G. Kresse, “Novel Stabilization Mechanism on Polar Surfaces: ZnO(0001)-Zn,” *Physical Review Letters*, vol. 90, p. 016102, Jan. 2003.

[17] A. Wander, F. Schedin, P. Steadman, A. Norris, R. McGrath, T. Turner, G. Thornton, and N. Harrison, “Stability of Polar Oxide Surfaces,” *Physical Review Letters*, vol. 86, pp. 3811–3814, Apr. 2001.

[18] M. Kunat, S. Gil Girol, T. Becker, U. Burghaus, and C. Wöll, “Stability of the polar surfaces of ZnO: A reinvestigation using He-atom scattering,” *Physical Review B*, vol. 66, p. 081402, Aug. 2002.

[19] A. Wander and N. M. Harrison, “An ab-initio study of ZnO(11 -2 0),” *Surface Science*, vol. 468, pp. L851–L855, Nov. 2000.

[20] K. Ozawa and K. Mase, “Comparison of the surface electronic structures of H-adsorbed ZnO surfaces: An angle-resolved photoelectron spectroscopy study,” *Physical Review B*, vol. 83, p. 125406, Mar. 2011.

[21] K. Ozawa and K. Mase, “Metallization of ZnO($10\bar{1}0$) by adsorption of hydrogen, methanol, and water: Angle-resolved photoelectron spectroscopy,” *Physical Review B*, vol. 81, p. 205322, May 2010.

[22] Y. Wang, B. Meyer, X. Yin, M. Kunat, D. Langenberg, F. Traeger, A. Birkner, and C. Wöll, “Hydrogen Induced Metallicity on the ZnO(101Â¯0) Surface,” *Physical Review Letters*, vol. 95, p. 266104, Dec. 2005.

[23] K. Ozawa and K. Mase, "Angle-resolved photoelectron spectroscopy study of hydrogen adsorption on ZnO$(10\bar{1}0)$," *physica status solidi (a)*, vol. 207, pp. 277–281, Feb. 2010.

[24] J.-C. Deinert, D. Wegkamp, M. Meyer, C. Richter, M. Wolf, and J. Stähler, "Ultrafast Exciton Formation at the ZnO(10-10) Surface," *Phys. Rev. Lett.*, vol. 113, p. 057602, July 2014.

[25] J.-C. Deinert, O. T. Hofmann, M. Meyer, M. Wolf, M. Scheffler, J. Stähler, and P. Rinke, "Hydrogen-induced metallisation at the ZnO$(10\bar{1}0)$ surface." to be published, 2014.

[26] V. P. Zhukov, P. M. Echenique, and E. V. Chulkov, "Two types of excited electron dynamics in zinc oxide," *Physical Review B*, vol. 82, p. 094302, Sept. 2010.

[27] D. Schneider, T. Rabe, T. Riedl, T. Dobbertin, O. Werner, M. Kröger, E. Becker, H.-H. Johannes, W. Kowalsky, T. Weimann, J. Wang, P. Hinze, A. Gerhard, P. StoÌˆssel, and H. Vestweber, "Deep blue widely tunable organic solid-state laser based on a spirobifluorene derivative," *Applied Physics Letters*, vol. 84, no. 23, p. 4693, 2004.

[28] M. Kemerink, S. Alvarado, P. Müller, P. Koenraad, H. Salemink, J. Wolter, and R. Janssen, "Scanning tunneling spectroscopy on organic semiconductors: Experiment and model," *Physical Review B*, vol. 70, p. 045202, July 2004.

[29] S. Blumstengel, S. Sadofev, C. Xu, J. Puls, R. Johnson, H. Glowatzki, N. Koch, and F. Henneberger, "Electronic coupling in organic-inorganic semiconductor hybrid structures with type-II energy level alignment," *Physical Review B*, vol. 77, p. 085323, Feb. 2008.

[30] S. Blumstengel, S. Sadofev, J. Puls, and F. Henneberger, "An inorganic/organic semiconductor "sandwich" structure grown by molecular beam epitaxy.," *Advanced materials (Deerfield Beach, Fla.)*, vol. 21, pp. 4850–3, Dec. 2009.

[31] N. Koch, "Organic electronic devices and their functional interfaces.," *Chemphyschem : a European journal of chemical physics and physical chemistry*, vol. 8, pp. 1438–55, July 2007.

[32] J. Stähler, O. T. Hofmann, P. Rinke, S. Blumstengel, F. Henneberger, Y. Li, and T. F. Heinz, "Raman study of 2,7-bis(biphenyl-4-yl-)2',7'-ditertbutyl-9,9'-spirobifluorene adsorbed on oxide surfaces," *Chemical Physics Letters*, vol. 584, pp. 74–78, Oct. 2013.

[33] L. Foglia, L. Bogner, M. Wolf, and J. Stähler, "Exciton trapping in vibrationally excited organic molecules near a ZnO surface," 2014.

[34] K. Christmann, *Introduction to Surface Physical Chemistry.* Springer Verlag, 1991.

[35] A. Einstein, "Über einen die Erzeugung und Verwandlung des Lichtes betreffenden heuristischen Gesichtspunkt," *Annalen der Physik*, vol. 322, no. 6, pp. 132–148, 1905.

[36] D. Wegkamp, "Schnelle Elektronendynamiken an Grenzflächen untersucht mit einer NOPA-basierenden Femtosekunden-Lichtquelle," Master's thesis, Freie Universität Berlin, Physics Department, 2009.

[37] J.-C. Deinert, "Zeit- und winkelaufgelöste Zweiphotonen-Photoemissionsspektroskopie: Aufbau und Charakterisierung des Experiments anhand der Cu(111)- und der D_2O/Cu(111)-Oberfläche," Master's thesis, Freie Universität Berlin, Physics Department, 2011.

[38] K. Fink, "Ab initio cluster calculations on the electronic structure of oxygen vacancies at the polar ZnO(000-1) surface and on the adsorption of H2, CO, and CO2 at these sites.," *Phys. Chem. Chem. Phys.*, vol. 8, pp. 1482–9, Apr. 2006.

[39] G. Sauerbrey, "Verwendung von Schwingquarzen zur Wägung dünner Schichten und zur Mikrowägung," *Zeitschrift für Phys.*, vol. 155, pp. 206–222, Apr. 1959.

Erklärung der Urheberschaft

Ich erkläre hiermit an Eides statt, dass ich die vorliegende Arbeit ohne Hilfe Dritter und ohne Benutzung anderer als der angegebenen Hilfsmittel angefertigt habe; die aus fremden Quellen direkt oder indirekt übernommenen Gedanken sind als solche kenntlich gemacht. Die Arbeit wurde bisher in gleicher oder ähnlicher Form in keiner anderen Prüfungsbehörde vorgelegt und auch noch nicht veröffentlicht.

Ort, Datum Unterschrift